Supplementary Information

Dynamic Coordinated Geminal-atom Catalyst for Highly Efficient Photo-Fenton Reactions

Yuchen Qiao[1], Su Zhan[1*], Qiuchen He[1], Kun Qi[2*], Yang Zhang[1], Jiangpeng Li[1], Wenjun Jiang[1], Keqiang Chen[3], Lanlu Lu[4], Damien Voiry[5] & Feng Zhou[1*]

[1] *Dalian Maritime University, Key Lab Ship. Machinery Maintenance & Manufacture, Minist. Transport, Dalian 116026, China*

[2] *State Key Laboratory of Catalysis, Dalian Institute of Chemical Physics, Chinese Academy of Sciences, Dalian National Laboratory for Clean Energy, Dalian 116023, Liaoning, China*

[3] *Faculty of Materials Science and Chemistry, China University of Geosciences, Wuhan 430074, China*

[4]*National Facility for Protein Science in Shanghai, Shanghai Advanced Research Institute, Chinese Academy of Sciences, Shanghai 201210, China*

[5]*Institut Européen des Membranes, IEM, UMR 5635, Université Montpellier, ENSCM, CNRS, Montpellier 34000, France*

[*]Email: zhans@dlmu.edu.cn (S. Zhan), kunqi@dicp.ac.cn (K. Qi) & zhoufeng@dlmu.edu.cn (F. Zhou)

Table of contents

Supplementary Methods

Materials and reagents.

Copper nitrate trihydrate ($Cu(NO_3)_2 \cdot 3H_2O$, ACS reagent), 7-Hydroxycoumarin ($C_9H_6O_3$) and coumarin ($C_9H_6O_2$) were purchased at Shanghai Macklin Biochemical Technology Co., Ltd. Urea (CH_4N_2O, ACS reagent), hydrogen peroxide (H_2O_2, 30 wt.%), isopropanol (C_3H_8O, ACS reagent), sodium chloride (NaCl, ACS reagent), silver nitrate ($AgNO_3$, ACS reagent), barium sulfate ($BaSO_4$, ACS reagent), sodium carbonate (Na_2CO_3, ACS reagent), sodium nitrate ($NaNO_3$, ACS reagent), sodium sulfate (Na_2SO_4, ACS reagent), potassium bromide (KBr, ACS reagent), potassium dihydrogen phosphate (KH_2PO_4, ACS reagent), n-hexane (C_6H_{14}, ACS reagent) were purchased at Tianjin Kemiou Chemical Reagent Co., Ltd. Nafion solution (5 wt.% in ethanol) was purchased from Adamas-beta. Diesel (No. 0 for sale) was purchased at China National Petroleum Corporation Limited, polyethylene microplastics (MPs, 50 mesh) was purchased from Dongguan Huaxin Plastic Co., Ltd. Fluorescein diacetate (FDA, $C_{24}H_{16}O_7$, ACS reagent), propidium iodide (PI, $C_{27}H_{34}N_4I_2$, ACS reagent) were purchased from Sigma Aldrich. H_2/Ar (H_2 5%(v/v)) was purchased at Dalian Guangming Special Gas Co., Ltd. Fresh seawater (pH ~ 7.7) was obtained from the Yellow Sea (121°54’E, 38°86’N).

Preparation of the catalysts.

Synthesis of CN.

Urea was dispersed in 50 mL of deionized (DI) water and sonicated for 30 minutes to ensure complete dissolution. The solution was then freeze-dried, and the resulting solid was thoroughly ground. The ground solid was placed in a covered crucible and heated to 500 °C at a ramping rate of 5 °C min^{-1} for 2 hours. After cooling to room temperature, a light yellow solid was obtained. The solid was ground again and acid-washed at room temperature to remove impurities. It was then rinsed with DI water until the waste solution reached a neutral pH. The purified solid was dried under vacuum at 50 °C for 12 hours, cooled to room temperature, and ground again and stored in Ar protection for further usage.

Synthesis of Cu_g-CN.

Urea was dispersed in 50 mL of deionized (DI) water, and copper nitrate was added based on the desired mass ratios of doped Cu (0.1%, 0.3%, 0.5%, 0.7%, 0.9%, and 1.2%). The mixture was sonicated for 30 minutes to ensure complete dissolution. The solution was then freeze-dried, and the resulting solid was thoroughly ground under vacuum conditions. Subsequently, 10 g of the ground

solid was evenly distributed in a ceramic crucible and heated to 500 °C in a H_2/Ar (5% H_2 by volume) atmosphere at a ramping rate of 5 °C min^{-1} for 2 hours. The resulting tan solid was ground again and acid-washed at room temperature to remove impurities. The precipitate was rinsed with DI water until the waste solution reached a neutral pH. Finally, the solid was dried under vacuum at 50 °C for 12 hours, cooled to room temperature, and ground into a fine powder. The samples were labelled as 0.1% Cu_g-CN, 0.3% Cu_g-CN, 0.5% Cu_g-CN, 0.7% Cu_g-CN, 0.9% Cu_g-CN, and 1.2% Cu_g-CN, corresponding to the mass percentage of Cu added in the precursor.

Material Characterization

Powder X-ray diffraction (XRD) was conducted using a Shimadzu XRD-6100 instrument with a Cu target (40 kV, 40 mA). Scans were performed over a 2θ range of 10° to 80° at a scanning speed of 8° min^{-1}. Scanning electron microscopy (SEM) was carried out on a ZEISS SUPRA 55 SAPPHIRE instrument operated at 3 kV. Fourier transform infrared spectroscopy (FT-IR) measurements were performed using a Thermo Fisher Nicolet IS 50 instrument. X-ray photoelectron spectroscopy (XPS) was performed on a Thermo Fisher Scientific K-Alpha system, with binding energy calibration using the C 1s peak at 284.8 eV. Specific surface area measurements via Brunauer-Emmett-Teller (BET) analysis were performed using a WBL-810 specific surface area and porosity analyzer with liquid nitrogen at 77.3 K. Transmission electron microscopy (TEM) and Energy-dispersive X-ray spectroscopy (EDX) analyses were performed using an FEI Talos F200S G2 Super-X instrument. HAADF-STEM images were acquired using a JEOL-ARM200F TEM operated at 200 kV. The attainable spatial resolution of the microscope was 78 pm with a probe spherical-aberration corrector. The images were acquired with an illumination semi-angle of 25 mrad and a probe current of 100 pA. The dwell time for image acquisition was set at 10 μs per pixel to ensure a desirable signal-to-noise ratio. The collection angles for the HAADF images were fixed at 90-250 mrad. To obtain high-quality scanning transmission electron microscopy (STEM) images with atomic resolution, the material was pre-treated at 60 °C in a vacuum oven for 4 h to remove any organic contaminants on its surface. A field-emission scanning electron microscope (TESCAN Mira3) was employed to observe the morphology of the samples. Aberration-corrected high-resolution (scanning) transmission electron microscopy (HR-(S)TEM) imaging and EDX spectroscopy were performed using an FEI Titan Cubed Themis microscope that was operated at 200 kV. The Themis microscope was equipped with a double Cs aberration corrector, a monochromator, an extreme field emission gun, a super EDX detector and

an ultra-high resolution energy filter (Gatan Quantum ERS) that allows for working in dual-range electron energy loss spectroscopy mode. HR-STEM imaging was performed using HAADF and annular dark-field detectors. Electron paramagnetic resonance (EPR) signals were detected using a Bruker EMXplus spectrometer (EMX-PLUS, Bruker, USA). UV-visible diffuse reflectance spectroscopy (UV-Vis DRS) was conducted using a Shimadzu UV2700i instrument, with $BaSO_4$ as a reference standard. High-temperature gel permeation chromatography (GPC) was performed using a PL-GPC220 system. Photoluminescence (PL) spectra were acquired using a PIXEA-CU-1 spectrometer (AUREA, France) at an excitation wavelength of 350 nm. Electrochemical testing was conducted on Correst CS310M EIS potentiostat. Femtosecond transient absorption (fs-TA) spectroscopy was performed using a coherent regeneratively amplified Ti:sapphire laser system (800 nm, 35 fs, 6 mJ/pulse, 1 kHz repetition rate) coupled with a Femto-TA100 spectrometer (Time-Tech Spectra) via nonlinear mixing technology.

Electrochemical Characterization

The electrochemical performance of the photocatalytic materials was evaluated using a standard classical three-electrode system. A 2 × 1 cm carbon fibre paper was applied as the working electrode (WE), KCl saturated Ag/AgCl as the reference electrode (RE) and a 2 × 1 cm Pt mesh as the counter electrode (CE), respectively. For the preparation of catalyst ink, 10 mg of catalyst was mixed with 20 mL of isopropanol and 50 μL of Nafion solution (5% wt. in ethanol). After gentle handshake, the catalyst ink was sonicated for 20 min to obtain a homogeneous solution. 100 μL of the catalyst ink was added dropwise on both sides of the carbon paper and subsequently dried under the illumination of an infrared lamp. Finally, the catalyst load on the working electrode was controlled as 1.0 mg cm^{-2}, which is comparable with the previous literature.

Hydroxyl Radical (·OH) Yield Assay.

The concentration of hydroxyl radicals (·OH) produced during the photo-Fenton process was measured using a fluorescence method with coumarin as a probe molecule.[1,2] Coumarin reacts with ·OH to form 7-hydroxycoumarin (7-HOC), which exhibits strong fluorescence at 455 nm, with the fluorescence intensity being proportional to the ·OH concentration. This method provides a simple, rapid, and sensitive approach for detecting ·OH in water. For the assay, 5 mg of the photo-Fenton catalyst was added to 50 mL of an aqueous solution containing 1 mM coumarin and homogenized. Subsequently, 1 mM H_2O_2 was introduced, exposing the solution to visible light (wavelength > 420 nm). Samples (3

mL) were taken for fluorescence intensity measurement during the reaction. The fluorescence intensity at 455 nm was recorded using an excitation wavelength of 340 nm. Based on the intensity and a standard curve for 7-HOC, the ·OH concentration was calculated using the following equation.[3,4]

$$[\bullet OH] = 2 \times [7-HOC]/Se \qquad (1)$$

where [7-HOC] and Se denote the concentration and selectivity of 7-HOC, respectively.

Labeling of 7-HOC: Before the concentration of ·OH radicals generated by the photo-Fenton reaction is measured, 7-HOC needs to be labeled. Coumarin is in excess during the photo-Fenton reaction, and to avoid the effect of coumarin on the fluorescence intensity of 7-HOC, 0.1 mM of coumarin was added as a background in the configuration of 7-HOC solutions at different concentrations. The fluorescence intensity of different concentrations of 7-HOC was subsequently measured to obtain a 7-HOC labeling line. As shown in Supplementary Figure 14, the concentration of 7-HOC had a good linearity with the fluorescence intensity when it was in the range of 0-5 μM. The fluorescence intensity of 7-HOC was measured in DI water and natural seawater with different concentrations, respectively. The effect of ions on the fluorescence intensity in complex environments was excluded (Supplementary Figure 15 to 16).

Inactivation of Chlorella.

Chlorella solution configuration.

Using Chlorella vulgaris as the inactivation target, Chlorella vulgaris was inoculated into autoclaved natural seawater with the addition of Na_2CO_3 (0.02 g L^{-1}), $NaNO_3$ (2 g L^{-1}), KH_2PO_4 (0.02 g L^{-1}), and urea (0.8 g L^{-1}). After one week of incubation in a light-constant incubator, the chlorella alga solution can be used.

Detection of chlorella.

50 mL of diluted Chlorella solution was taken into a flow reactor and sampled after 7 min of cycling under Xenon lamp. Chlorella survival was observed using fluorescence staining (FDA and PI staining solution).[5–7] The circulating algal solution was centrifuged for 5 min and washed with DI water; afterward the fluorescence staining solution was added, mixed thoroughly, and allowed to stand in a dark environment for 10 min. Next, the stained algal solution was centrifuged, and the supernatant was removed added with DI water, and centrifuged again. After centrifugation three times, the solution

diluted by the addition of phosphate-buffered saline. The stained algal solution was placed on a hematocrit plate and the cells were observed under a fluorescence microscope at 40× magnification. The inactivation rate was obtained according to following Eq. (2) :

$$\text{Inactivation rate}(\%) = \frac{C_0 - C_t}{C_0} \times 100\% \qquad (2)$$

where C_0 is the number of active chlorella and C_t is the number of inactive chlorella.

Degradation of diesel experiment.

Establishment of standard curve.

Different volumes of diesel oil were added to n-hexane solution, mixed, and the absorbance of diesel oil with different concentrations was measured by ultraviolet spectrophotometer at 225 nm, and the straight line shown in Supplementary Figure 24 was fitted to obtain a good linear relationship between absorbance and diesel oil concentration.

Calculation of the degradation rate for diesel.

The seawater solution containing 0.1 g L^{-1} diesel fuel, supplemented with 0.1 g L^{-1} catalyst and 0.004 M H_2O_2, was subjected to 1 h of light exposure under a Xenon lamp, with continuous stirring provided by a magnetic stirrer throughout the exposure period. After the photocatalytic reaction, the oil is separated from the seawater by extraction using n-hexane as the extraction reagent. Then the resulting oil solution was diluted to a certain multiple, and then the absorbance was determined at 225 nm wavelength with n-hexane as the reference. The remaining oil content can be obtained by converting the obtained absorbance to the corresponding standard curve. The degradation rate was obtained according to following Eq. (3) :

$$\text{Degradation rate}(\%) = \frac{O_0 - O_t}{O_0} \times 100\% \qquad (3)$$

where O_0 represents the initial amount of diesel oil and O_t represents the amount of diesel left.

Experiment for the degradation of microplastic.

3.0 g of polyethylene plastic microspheres were immersed in seawater, followed by adding 2.0 g catalyst and 100 μL H_2O_2, and then stirred under a Xenon lamp for 12 h. The solution was subsequently filtered, and the resulting solids were thoroughly washed with DI water, centrifuged, and finally dried to yield degraded polyethylene microplastics. By conducting GPC test on polyethylene microplastics

before and after the reaction, the molecular weight of microplastics can be obtained, and the degradation rate of microplastics can be calculated. The degradation rate was obtained according to following Eq. (4) :

$$\text{Degradation rate}(\%) = \frac{M_0 - M_t}{M_0} \times 100\% \qquad (4)$$

where M_0 represents the number average molecular weight of polyethylene microplastics before the reaction, and M_t represents the number average molecular weight of polyethylene microplastics after the reaction.

***Ex-situ* and *Operando* X-ray absorption spectroscopy measurements.**

Ex-situ and *Operando* X-ray absorption spectroscopy (XAS) for Cu K-edge data were collected at room temperature at Shanghai Synchrotron Radiation Facility (SSRF) on beamline BL13SSW equipped with a double-crystal Si (111) monochromator at the Cu K-edge for energy selection. The beam size was 1.0 × 0.5 mm. The signals were collected in fluorescence mode using a 13-channel Ge detector. The intensity of the incident radiation was measured with an ionization chamber (I_0) filled with an N_2 (500 mbar) / He (500 mbar) mixture. Two additional ionization chambers filled with 1700 mbar N_2 (in I_1 chamber) and an Ar (150 mbar) / N_2 (850 mbar) mixture (in I_1 chamber) were used for measurements in transmission mode in the case of the reference samples. The energy resolution (ΔE / E) for the incident X-ray photons was estimated to be 2.0×10^{-4}. A custom-designed photo-electrochemical cell (Zahner, PECC-2) was used for the *operando* Cu-K edge XAS measurements. The applied potential was controlled by a VSP potentiostat (Bio-Logic Science Instruments). For the *operando* XAS studies, the catalyst ink was drop casted on the surface of gas diffusion layer (GDL, Sigracet 22 BB, Fuel Cell Store). The GDL was then mounted on a graphite foil by polyamide tape as both a working electrode and window for the pass-through of the X-ray. Time-resolved spectra were recorded every 10 mins, to ascertain the reproducibility of the experimental data, at least three scan sets were collected and compared for each sample.

Extended X-ray absorption fine structure curve fitting and data analysis.

Extended X-ray absorption fine structures (EXAFS) curve fitting and data analysis were performed with the Artemis and IFEFFIT software. Standard data-processing, including energy calibration and spectral normalization of the raw spectra was performed using the Athena program. Each sample of XAS data was aligned and processed using the Athena program. Spectra were baseline corrected using

a linear pre-edge function between -200 and -50 eV and normalized using a linear or quadratic function between 150 and 700 eV, including a flattening function in the post-edge region. To track the copper valence state distribution, a linear combination fitting analysis, included in Athena, was carried out using the hXAS spectra of various copper-based standards. The XAFS signal was isolated from the adsorption edge background using a fit to a cubic spline with nodes defined by the AUTOBKG function in IFEFFIT, with a *k*-weight of 3 and with the Rbkg parameter set to 1. Fourier transformations of k^3-weighted spectra were using a Kaiser-Bessel window with a 1 $Å^{-1}$ sill width. The magnitude parts of the Fourier transformed spectra are shown throughout this manuscript with a radial distance scale that is not corrected for phase shift. For EXAFS fitting, theoretical scattering paths were calculated with FEFF6 using Artemis. All EXAFS spectra (*in-situ* and *ex-situ*) were fit for distances (ΔR), coordination number (CN), and mean-square displacement of interatomic distance (σ^2) using the Artemis interface with a fixed amplitude reduction factor (S_0^2) of 0.707 to 1.000. The parameters such as interatomic distance (R), CN, the difference in threshold energy (ΔE_0) and Debye-Waller factor (σ^2) were first established with reasonable guesses and then were fitted in R-space. The error in the overall fits was determined using the R-factor, the goodness-of-fit parameter, in which R-factor = $\Sigma(\chi_{data} - \chi_{fit})^2$ / $\Sigma(\chi_{data})^2$ and good fits occur for R-factor < 0.05. For the wavelet transform analysis, the χ(k) exported from Athena was imported into the Hama Fortran code available on the European Synchrotron Radiation Facility (ESRF) website. The parameters were listed as follow: R range = 1 to 4 Å, *k* range = 0 to 13 $Å^{-1}$; *k* weight = 2 and Morlet function with $k = 10$, $\sigma = 1$ was used as the mother wavelet to provide the overall distribution.

Raman spectroscopy measurements.

In situ Raman measurements of catalysts were carried out with a Mettler-Toledo React Raman 802L spectrometer. H_2O_2 at a concentration of 1 mmol L^{-1}, NaCl solution at 0.5 mmol L^{-1}, and Na_2CO_3 solution at 0.24 mmol L^{-1} were sequentially added to the reaction cell containing the catalyst for testing. In situ Raman spectra were collected at consistent time intervals by inserting the Raman probe below the liquid level on the catalyst surface under xenon lamp (wavelength > 420 nm) irradiation. Prior to each solution change, the Raman probe surface was thoroughly cleaned to eliminate any residual ions that could potentially interfere with subsequent tests. Raman data was analyzed using the iC Raman (version 8.0) software.

Computational Methods.

To study the decomposition of H_2O_2 on Cu sites in the Cu-g-CN system, a simulation experiment was

designed by adding H_2O_2 molecules. To investigate the effect of CO_3^{2-} ion adsorption on H_2O_2 decomposition, CO_3^{2-} is preferentially adsorbed on the Cu site in the form of bridge adsorption. This carbonate adsorption facilitates the decomposition of H_2O_2 into H^+ and *OOH. The formation of Cu-OOH is favorable for the selective conversion of hydrogen peroxide into hydroxyl radicals, which aligns well with the experimental results. This process enhances the efficiency of H_2O_2 decomposition and supports the generation of hydroxyl radicals, demonstrating the catalytic activity of Cu sites in the presence of CO_3^{2-} ions.

DFT Calculation detail.

The DFT calculations were expanded using the projected augmented wave (PAW) basis set.[8,9] The study employed the generalized gradient approximation (GGA) with the Perdew-Burke-Ernzerhof (PBE) exchange-correlation functional to capture the exchange-correlation effects accurately. Adsorption geometries were optimized using a force-based conjugate gradient algorithm, ensuring that atomic positions were fully relaxed. Additionally, transition states were located using a constrained minimization technique to identify the highest energy points along the reaction pathways. The calculations were performed with a plane wave truncation energy of 520 eV, and the total system energy was maintained at less than 1.0×10^{-5} eV to ensure precision. For the Cu (002) surface, a (2×2) cell model was used, and k-point sampling was conducted using a $2 \times 2 \times 1$ grid centered at the gamma point to represent the Brillouin zone accurately.

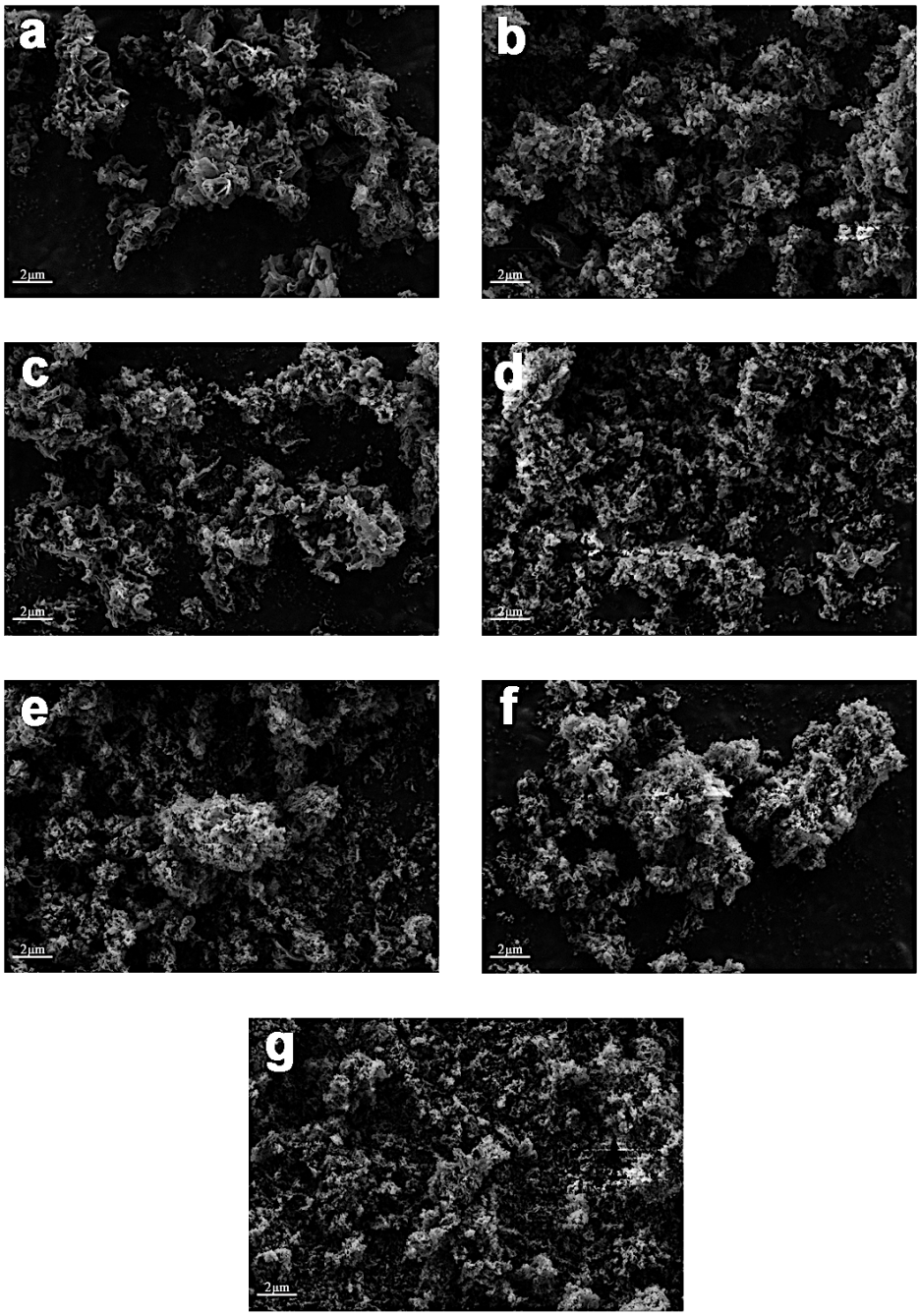

Supplementary Figure 1 | SEM characterization of the CN and Cu_g-CN catalyst. a, CN. **b**, 0.1% Cu_g-CN. **c**, 0.3% Cu_g-CN. **d**, 0.5% Cu_g-CN. **e**, 0.7% Cu_g-CN. **f**, 0.9% Cu_g-CN. **g**, 1.2% Cu_g-CN.

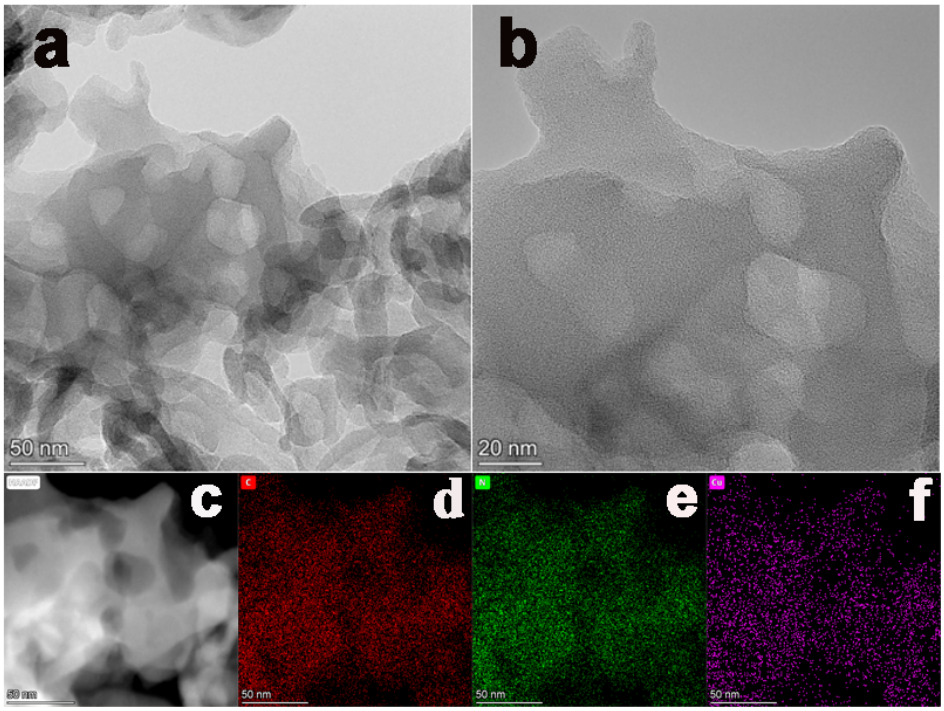

Supplementary Figure 2 | TEM and EDX-mapping characterization of the 0.7% Cu_g-CN **catalyst. a-b**, TEM images of the 0.7% Cu_g-CN. **c-f**, Corresponding element distribution of the 0.7% Cu_g-CN. Red: carbon, green: nitrogen and purple: copper.

Supplementary Note 1 | As shown in Supplementary Figure 2, the TEM images of 0.7% Cu_g-CN reveal that the prepared samples exhibit a two-dimensional nanosheet laminar structure. Notably, no lattice fringes corresponding to Cu monomers or Cu oxides were observed. This confirms the absence of Cu monomers and Cu oxide particles in the 0.7% Cu_g-CN sample.

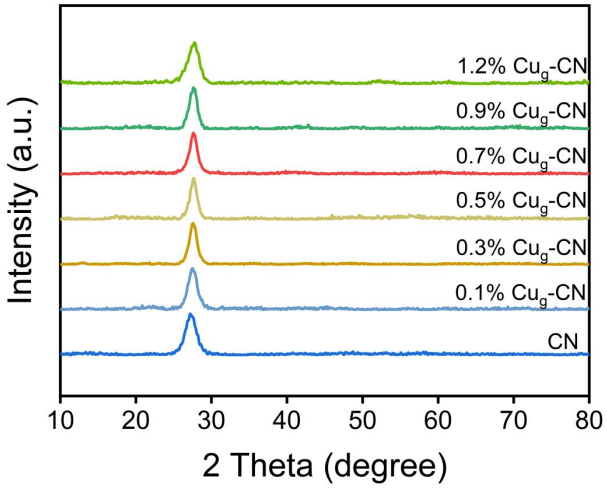

Supplementary Figure 3 | XRD spectra of the geminal atom catalyst with different Cu concentrations.

Supplementary Note 2 | As shown in Supplementary Figure 3, the XRD peak of Cu_g-CN is slightly shifted to the right at $2\theta = 27.2°$ compared to CN. This shift likely results from the successful doping of Cu onto the repetitive stack of tri-s-triazine units. However, the diffraction peaks of metallic Cu are not noticeably observed in any of the samples, suggesting that Cu is uniformly dispersed within the CN structure.

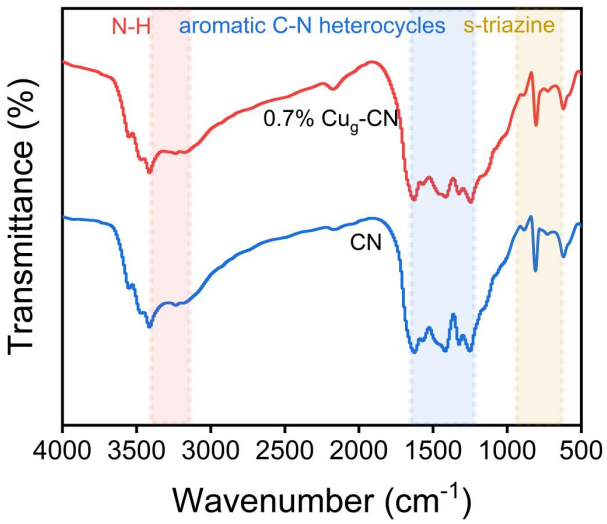

Supplementary Figure 4 | FT-IR spectra of CN and 0.7% Cu$_g$-CN.

Supplementary Note 3 | As shown in Supplementary Figure 4, both CN and Cu$_g$-CN samples exhibit the characteristic vibrational absorption peaks of the s-bis-triazine unit (800 cm^{-1}), aromatic C-N heterocycles (1250-1625 cm^{-1}), and N-H stretching (3080-3300 cm^{-1}).[10] However, the peak intensities of the C-N vibrational absorption peaks (at 1248 and 1416 cm^{-1}) in Cu$_g$-CN are slightly reduced. This reduction likely results from the successful doping of Cu atoms into the CN structure, forming bonds with the atoms in CN. Additionally, the absence of characteristic absorption peaks for Cu-O bonding at 530 cm^{-1}, 580 cm^{-1}, and 620 cm^{-1} suggests that Cu may be bonded to the CN skeleton in other configurations, rather than forming copper oxide phases.[11]

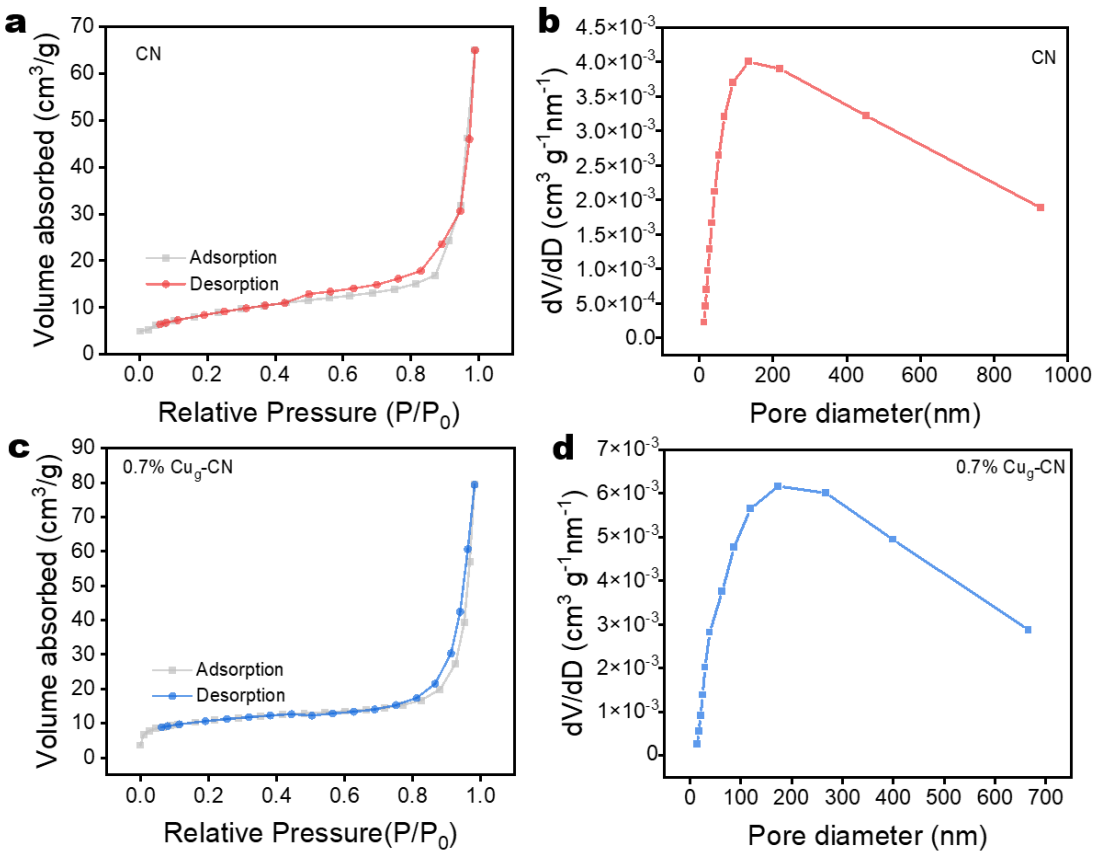

Supplementary Figure 5 | BET-specific surface area data of CN and 0.7% Cu_g-CN. a-d, N_2 adsorption-desorption isothermal curves and **c-d**, pore size distribution plots.

Supplementary Note 4 | The specific surface area of CN was 30.85 m^2/g (Supplementary Figure 5 a-b) and that of 0.7% Cu_g-CN was 37.14 m^2/g (Supplementary Figure 5 c-d). the formation of Cu monoatoms will not significantly change the catalyst-specific surface area and pore size distribution.

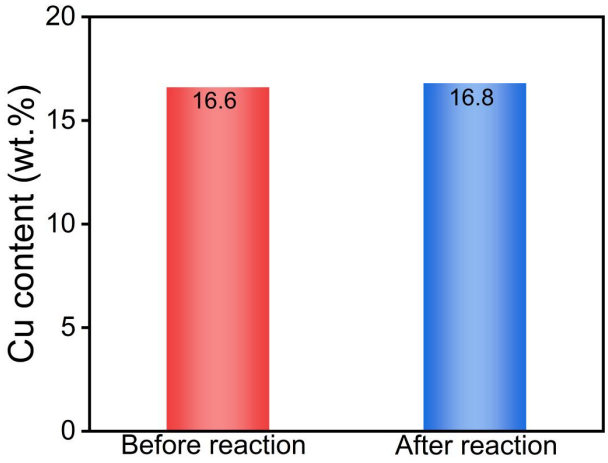

Supplementary Figure 6 | ICP-OES results of 0.7% Cu_g-CN catalyst before and after reaction.

Supplementary Note 5 | Supplementary Figure 6 shows that the Cu content in the 0.7% Cu_g-CN catalyst remains unchanged after the reaction compared to before the reaction. This indicates that the Cu-N bonding within the catalyst is highly stable, preventing significant Cu leaching into the solution.

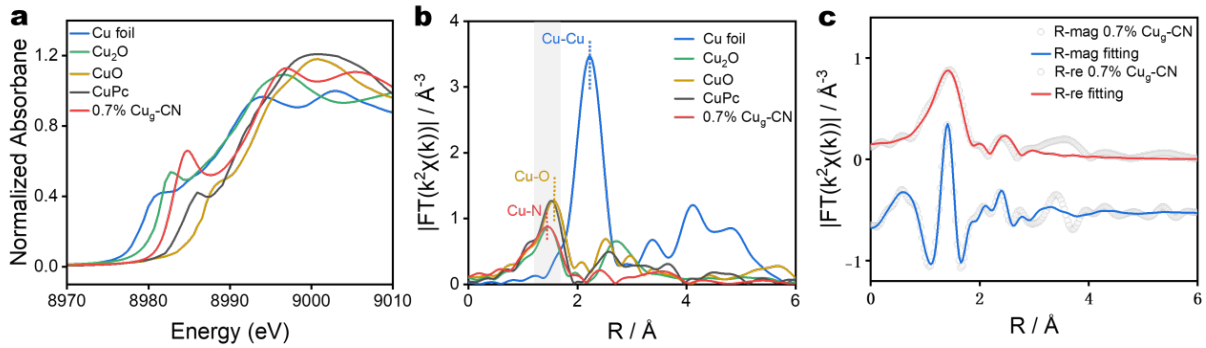

Supplementary Figure 7 | Validation of the XANES fitting and hard X-ray absorption spectroscopy (hXAS) characterization of the Cu-based standard samples. a, Cu K-edge XANES spectra of 0.7% Cu_g-CN, Cu foil, Copper(II) phthalocyanine (CuPc), CuO, and Cu_2O. **b**, FT-EXAFS spectra of 0.7% Cu_g-CN. **c**, the χ(R) space spectra fitting curved for 0.7% Cu_g-CN.

Supplementary Note 6 | X-ray absorption fine structure (XAFS) analysis was conducted to precisely determine the Cu's coordination environment in the catalyst. The X-ray absorption near edge structure (XANES) spectrum of the catalyst is presented in Supplementary Figure 7a. The K-edge signals and major jump energies of Cu in 0.7% Cu_g-CN indicate that its absorption threshold lies between those of CuO and Cu_2O, closely resembling the standard spectrum of Cu_2O. This observation suggests that Cu predominantly exists in the +1 valence state in Cu_g-CN, aligning with the previously discussed XPS results.[12,13] Detailed K-edge fitting parameters for Cu are provided in Supplementary Table 1. The Fourier transform extended X-ray absorption fine structure (FT-EXAFS) spectrum of 0.7% Cu_g-CN, shown in Supplementary Figure 7b, displays a single main peak at 1.44 Å. This peak corresponds to the scattering of the Cu-N bond, as seen in CuPc, while no coordination peaks are observed at 1.56 Å or 2.23 Å, which are associated with the Cu-Cu bond (Cu foil) and Cu-O bond (CuO), respectively.[14,15] These results confirm the successful synthesis of Cu monoatomic catalysts.

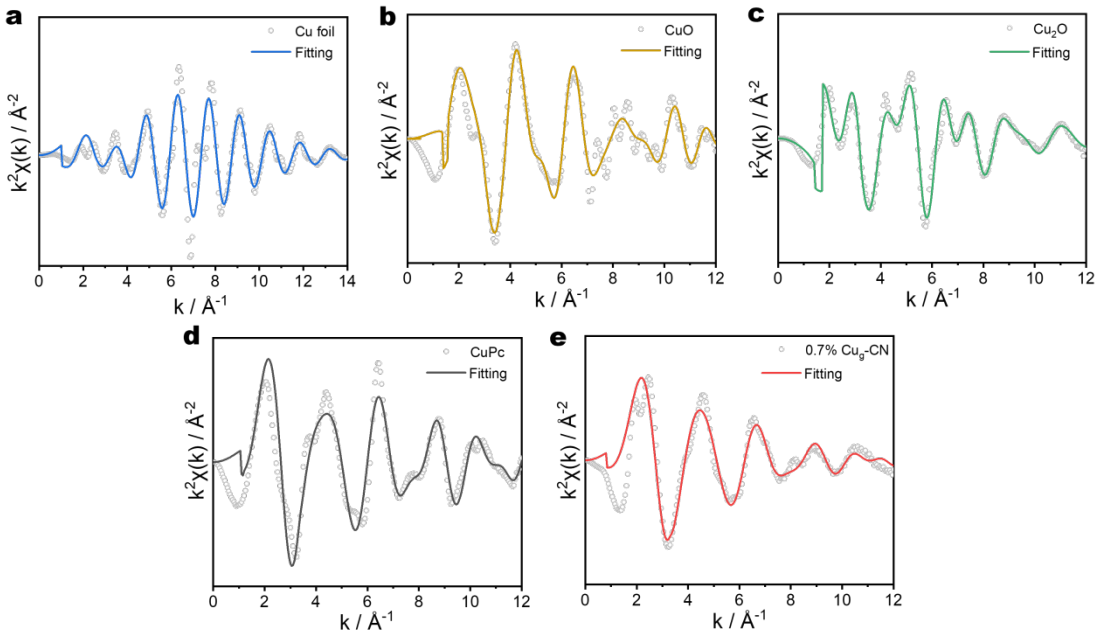

Supplementary Figure 8 | Potential-resolved Fourier-transformed magnitude of Cu samples K-edge **EXAFS spectra in K space and corresponding fitting results.** K-space fitting curves of **a**, Cu foil. **b**, CuO. **c**, Cu_2O. **d**, CuPc and **e**, 0.7% Cu_g-CN, respectively.

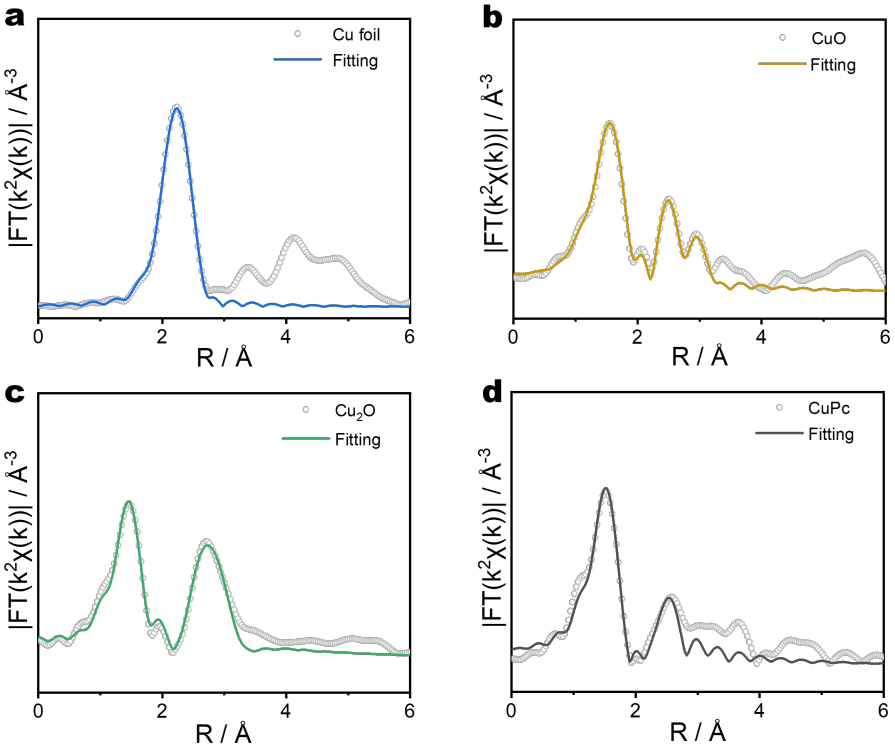

Supplementary Figure 9 | Potential-resolved Fourier-transformed magnitude of Cu samples K-edge **EXAFS spectra in R space and corresponding fitting results. a-d**, R-space fitting curves of Cu foil, CuO, Cu_2O and CuPc.

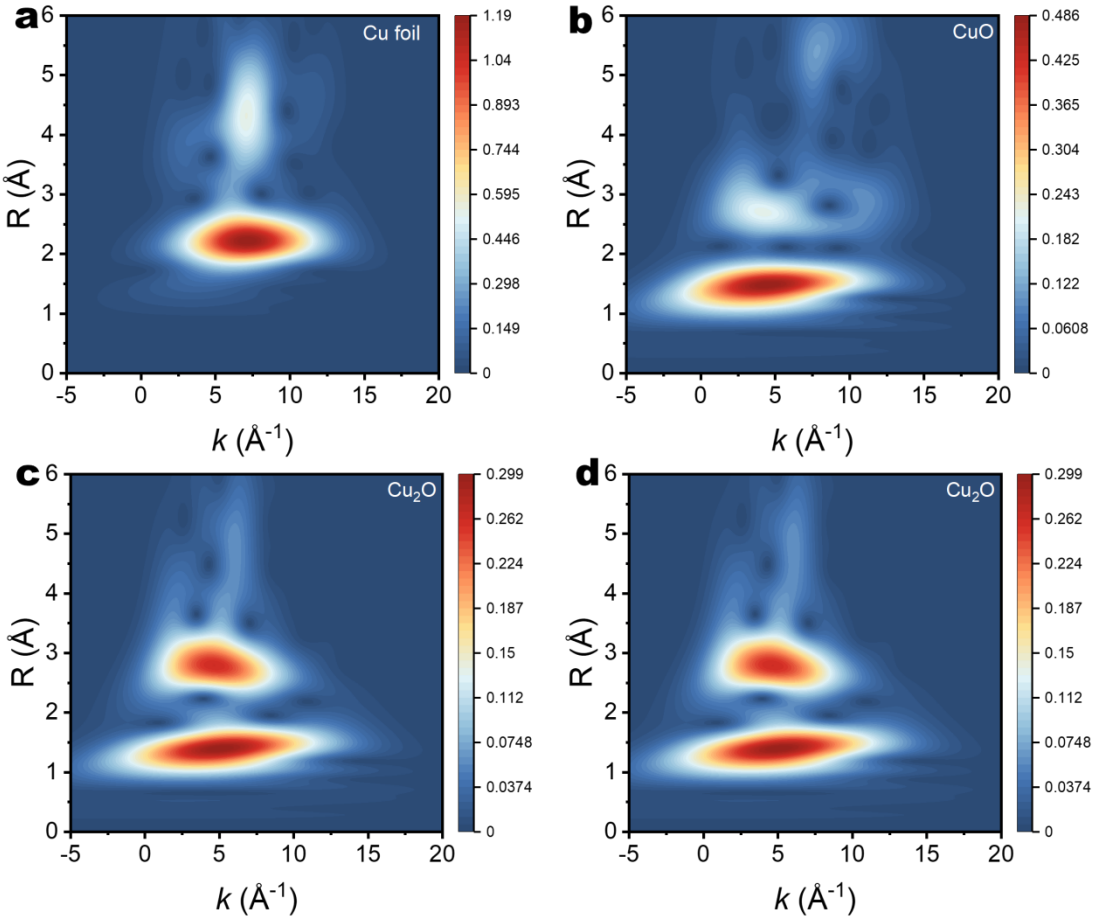

Supplementary Figure 10 | Cu K-edge **WT-EXAFS contour plots for the corresponding standard samples. a**, Cu foil. **b**, CuO. **c**, Cu_2O and **d**, CuPc.

Supplementary Table 1 | Curve fitting parameters obtained from Supplementary Figure 7 for the Cu K-edge EXAFS of the catalyst and standard samples.

Sample	Path	CN	R(Å)	σ^2($\times10^{-3}$Å^2)	ΔE_0 (eV)	R factor (%)
Cu foil	Cu-Cu	12	2.54±0.01	8.5±0.4	4.0±0.6	0.004
CuO	Cu-O	3.2±0.3	1.95±0.01	5.2±2.8	7.4±1.4	0.01
	Cu-Cu	11.3±0.9	3.05±0.01	2.1±1.8	2.3±3.7	
Cu_2O	Cu-O	4.2±0.6	1.87±0.01	5.0±4.8	-2.7±2.1	0.13
	Cu-Cu	10.1±0.7	3.01±0.01			0.18
CuPc	Cu-N	4.2±0.3	1.92±0.01	5.1±2.7	1.2±4.1	0.26
	Cu-C	7.5±0.4	2.94±0.01	3.2±6.1		
0.7% Cu_g-CN	Cu-N	2.3±0.4	1.90±0.01	9.1±2.7	2.7±2.9	0.018
	Cu-C	1.7±1.4	2.87±0.01	0.1±7.9		

N, coordination number; R, distance between absorber and backscatter atoms; σ^2, Debye-Waller factor to account for both thermal and structural disorders; ΔE_0, inner potential correction; R factor (%) indicates the goodness of the fit. Error bounds (accuracies) that characterize the structural parameters obtained by EXAFS spectroscopy were estimated as N ± 20 %; R ± 1 %; σ^2 ± 20 %; ΔE_0 ± 20 %. $S0^2$ = 0.91 was obtained by Cu foil fitting and applied for the other samples fitting. Fitting range: 3.0 ≤ k (Å^{-1}) ≤ 12.0 and 1.0 ≤ R (Å) ≤ 3.0.

Supplementary Note 7 | To further verify the coordination environment of Cu in the 0.7% Cu_g-CN sample, Cu K-edge EXAFS analysis was conducted. The results revealed no significant Cu-Cu or Cu-O bonds formation in the sample. This finding confirms the presence of a CuN_2 structure, formed through the coordination of isolated Cu atoms with nitrogen.

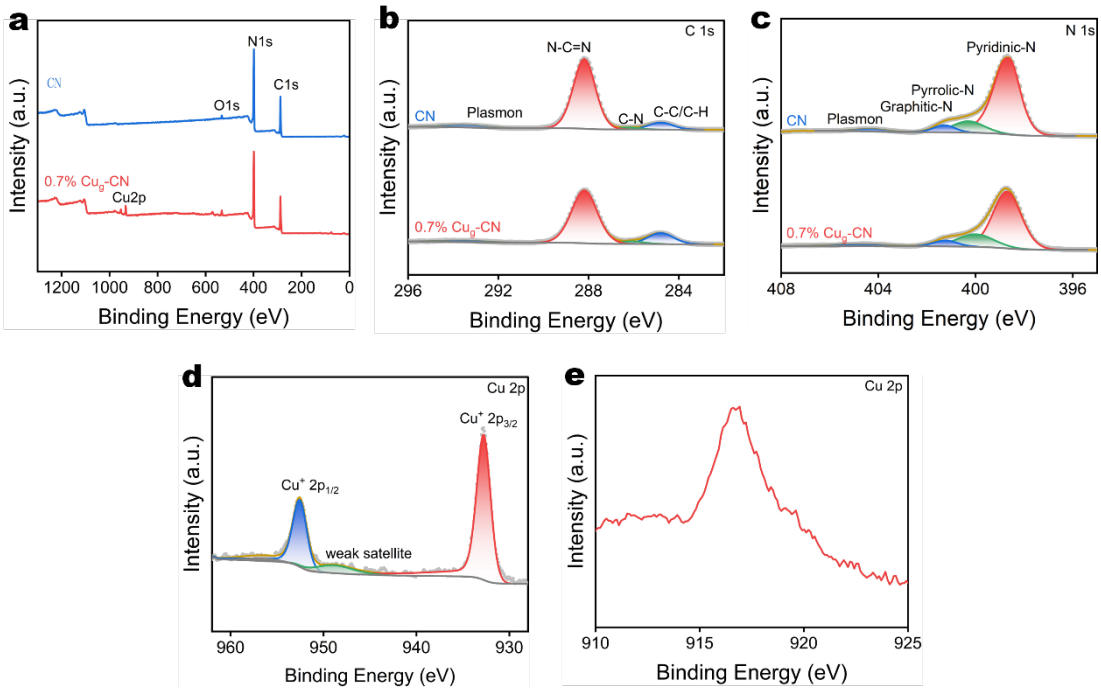

Supplementary Figure 11 | XPS spectra comparisons of CN and 0.7% Cu$_g$-CN. a, survey. **b**, C 1s. **c**, N 1s **d**, Cu 2p and **e**, Cu LMM Auger spectrum image of Cu$_g$-CN.

Supplementary Note 8 | As illustrated in Supplementary Figure 11c, the central peaks at 398.63 eV, 400.29 eV, and 401.29 eV in the N1s spectra correspond to pyridinic-N, pyrrolic-N, and graphitic-N, respectively. Pyridinic-N is recognized as a key coordination site for metal monoatoms.[16,17] The prepared catalyst contains a significant amount of pyridinic-N, which facilitates the formation of a Cu-N coordination structure. Notably, the pyridinic-N peak of 0.7% Cu$_g$-CN (399.24 eV) shifted to a higher binding energy compared to that of CN (398.63 eV). This shift may be attributed to lower electron density in the pyridinic-N coordination, as the sp²-hybridized N atoms in 0.7% Cu$_g$-CN donate electrons to the Cu 3d orbitals, forming the Cu-N coordination bond.[18] In the high-resolution XPS spectra of Cu 2p, the binding energies at 932.77 eV and 952.56 eV are assigned to Cu 2p$_{3/2}$ and Cu 2p$_{1/2}$, respectively, as shown in Supplementary Figure 11d.[19] Cu LMM Auger spectroscopy was conducted for the 0.7% Cu$_g$-CN material to further elucidate the valence states of the Cu species. A single peak at 916.57 eV, observed in Supplementary Figure 11e, confirms that the Cu species in the Cu$_g$-CN system exist predominantly in the +1 oxidation state.[20]

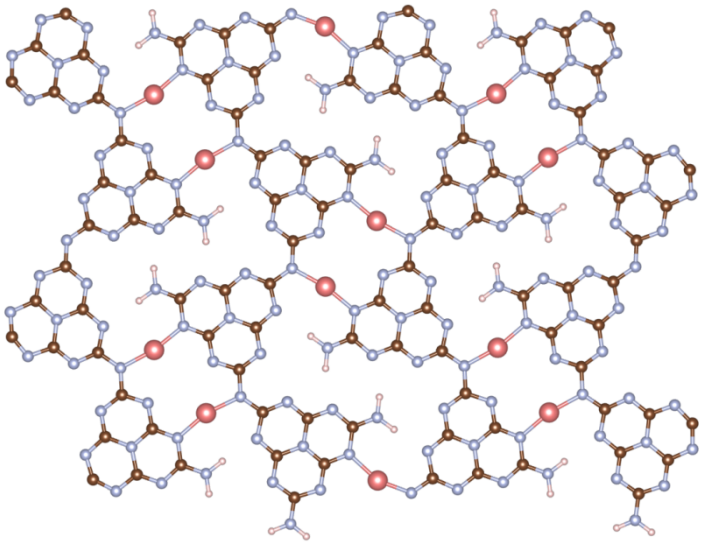

Supplementary Figure 12 | The atomic structure of 0.7% Cu_g-CN used for the XANES spectrum fitting.

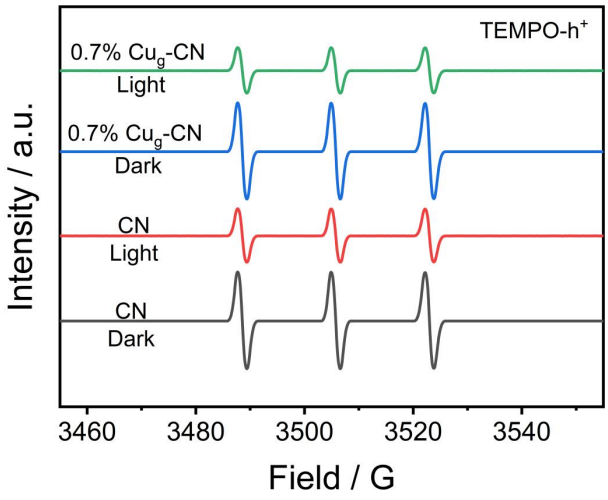

Supplementary Figure 13 | EPR spectra of TEMPO-h$^+$ in different catalytic systems.

Supplementary Note 9 | Supplementary Figure 13 shows no significant difference in the photogenerated hole signals between CN and 0.7% Cu_g-CN. This indicates that both materials generate a similar number of holes under light conditions, suggesting comparable light-absorbing properties and an analogous initial photogenerated carrier generation process.[21]

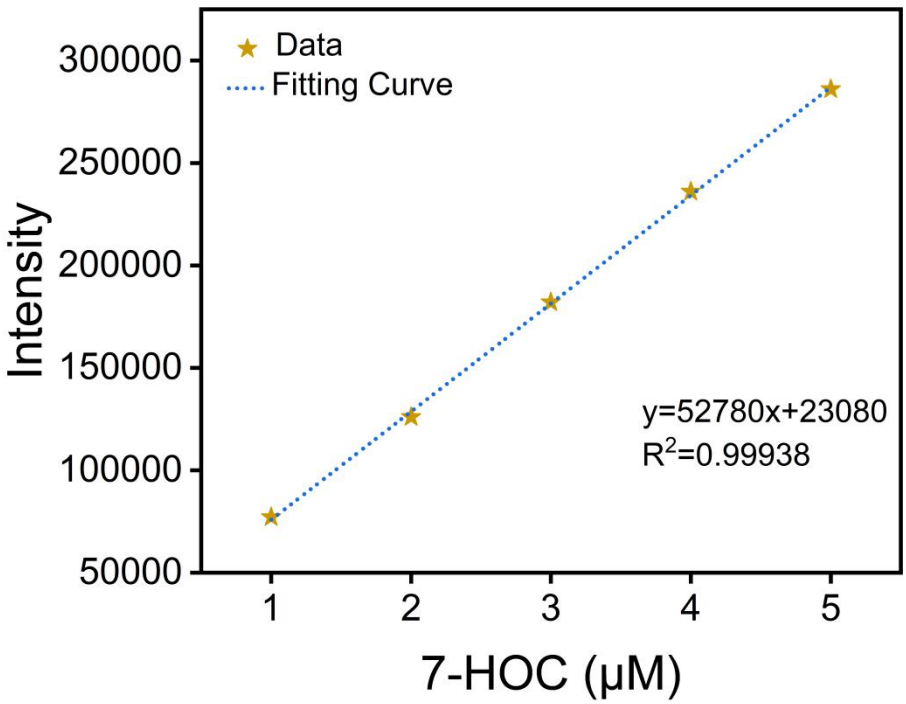

Supplementary Figure 14 | Calibration curve for the 7-HOC concentration to fluorescence intensity.

Supplementary Note 10 | The fitting curve represents the relationship between the concentration of 7-HOC and its corresponding fluorescence intensity, providing a quantitative analysis tool for concentration determination. By plotting the fluorescence intensity as a function of 7-HOC concentration, a linear correlation is observed within a specific concentration range, demonstrating the reliability and sensitivity of the fluorescence detection method. This curve serves as a standard for accurately measuring unknown concentrations of 7-HOC in various solution systems and highlights the consistency of fluorescence responses in different environmental conditions.

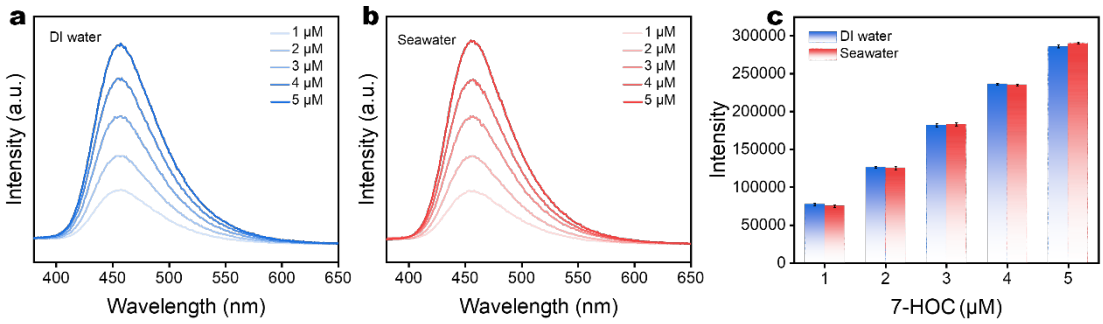

Supplementary Figure 15 | Fluorescence intensity of 7-HOC at different solutions with variable concentrations. **a-b**, DI water and seawater. **c**, Fluorescence intensity of different concentrations of 7-HOC with at 455 nm in DI water and seawater.

Supplementary Note 11 | As shown in Supplementary Figure 15, the fluorescence intensity of heptahydroxyl at the same concentration in DI water and seawater is consistent. This indicates that the complex ionic composition of seawater does not interfere with the fluorescence detection of 7-HOC.

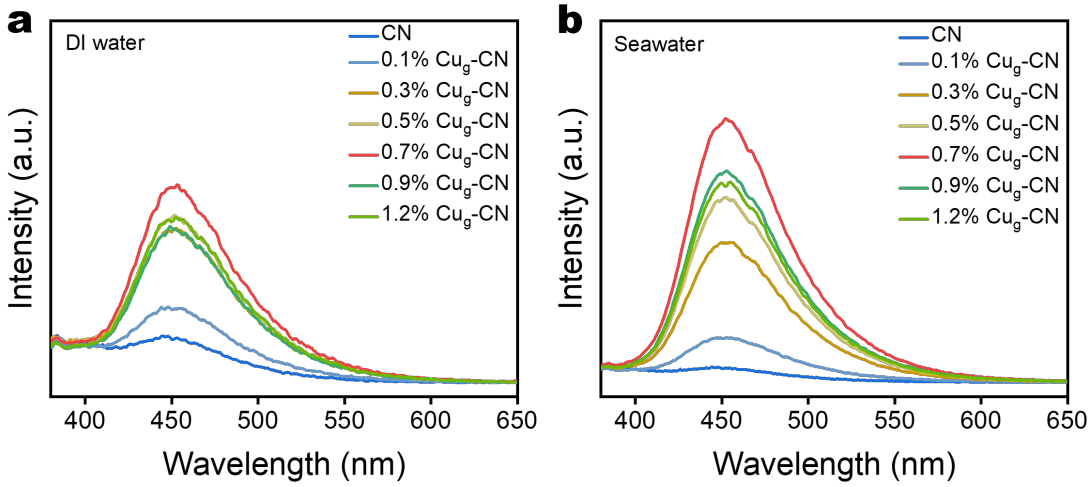

Supplementary Figure 16 | Fluorescence intensity of CN and Cu$_g$-CN in different solutions. a, DI water. **b**, seawater.

Supplementary Note 12 | As shown in Supplementary Figure 16, the strongest fluorescence peak intensity of heptahydroxycoumarin was observed at 455 nm for the 0.7% Cu$_g$-CN sample after the reaction in both DI water and seawater. This indicates that both DI water and seawater exhibit excellent ·OH-producing capabilities.

Supplementary Table 2 | The ·OH yield of 0.7% Cu_g-CN compared to other catalysts.

Sample	·OH production rate (μmol g^{-1} h^{-1})	Solution	H_2O_2 concentration (mM)	References
$CuFe_2O_4$	39.75	H_2SO_4	10	22
MIL-53(Cu)	15	H_2SO_4	10	23
HS-$CuFe_2O_4$-σ	35.25	HCl	40	24
Cu_5/FeS_2	240	-	0.8	25
meso-$CuFe_2O_4$	89.68	H_2SO_4	40	26
nano-Fe_3O_4	58.1	H_2SO_4	40	26
FeOF	1764.5	-	10	27
Cu-Fe_2O_3	2005	DI water	10	28
RF/RM	180	DI water	0.5	29
P-Cu-Al_2O_3	96.63	TPA	10	30
ZrO_2-Fe_2O_3	47.26	-	10	31
CD-COOFe(III)	1162.5	-	0.5	32
FeOCl	55	TPA	15	33
$BiFeO_3$	117	H_2SO_4	10	34
Ferrihydrite	75	-	10	35
DBC-FeO_x	526.4	-	2	36
ZVI	53.3	-	-	37
Ti_3C_2	4.5	-	4	38
SA-Co-CN/g-C_3N_4	2500	-	PMS	39
FeN_4-HPC	1725	Na_2SO_4	-	40
CN-FeNi-P	600	-	49	41
0.7% Cu_g-CN	**3240**	**Natural seawater**	**1**	**This work**

Supplementary Note 13 | To facilitate a meaningful comparison of ·OH yields, both the reaction time and the catalyst dosage were normalized across all samples. This normalization ensures that the observed differences in ·OH production rate is attributable solely to the intrinsic activity of the catalysts, eliminating the influence of variations in reaction conditions. By standardizing these parameters, a direct and reliable assessment of the ·OH production rate of the 0.7% Cu_g-CN catalyst under identical experimental conditions in both deionized water and seawater can be achieved.

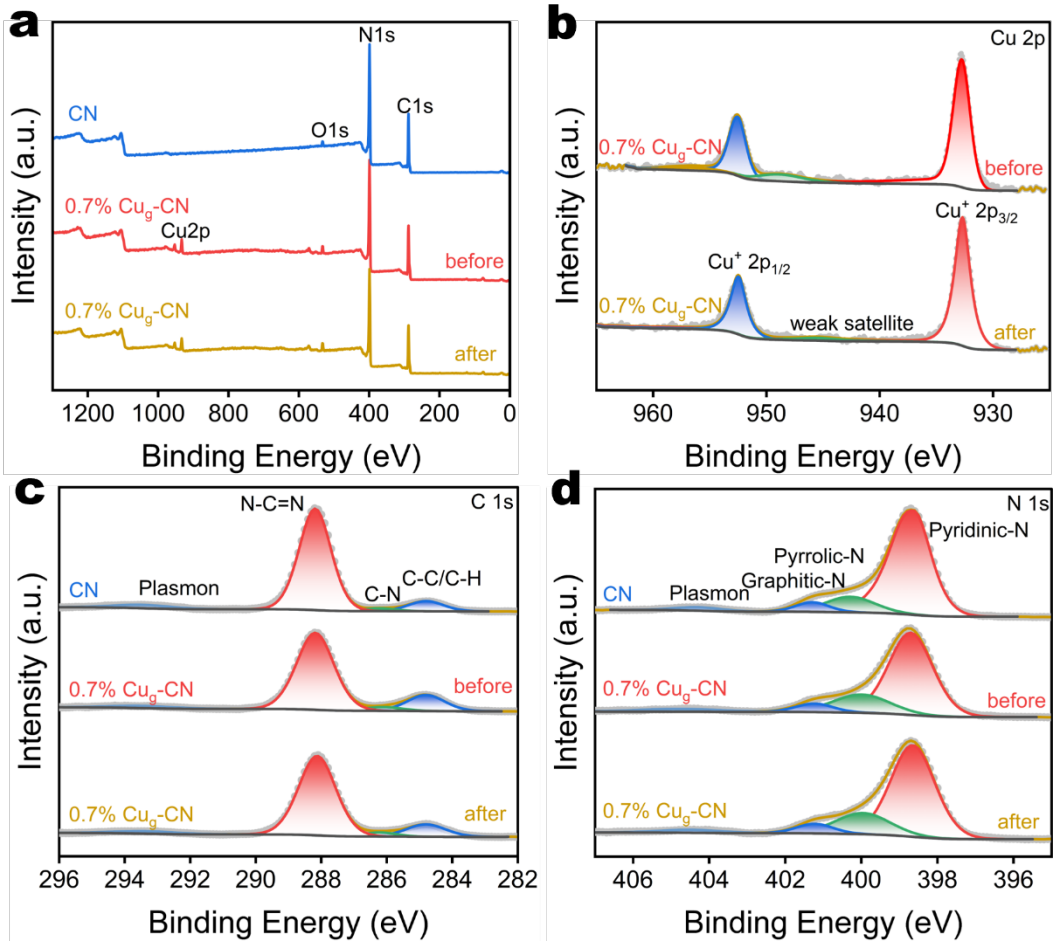

Supplementary Figure 17 | XPS spectra of the CN, together with 0.7% Cu$_g$-CN before and after the reaction. **a**, Survey. **b**, C 1s. **c**, N 1s and **d**, Cu 2p.

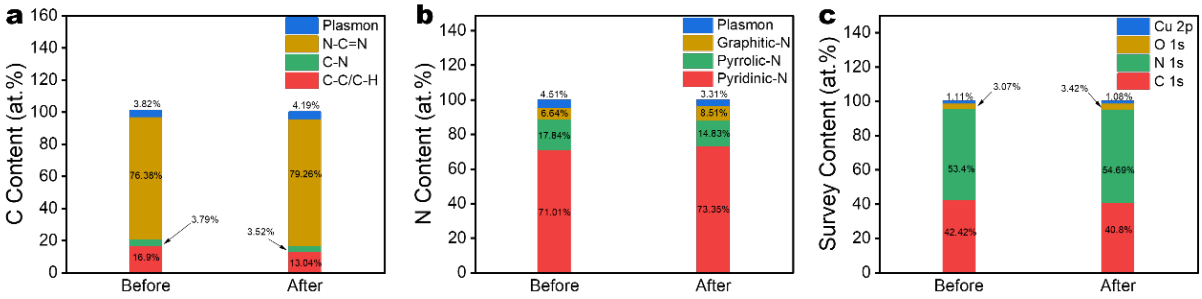

Supplementary Figure 18 | High-resolution XPS spectrum of the proportion of before and after reaction 0.7% Cu_g-CN. a-b, C 1s and N 1s. **c**, the elemental content (atom%).

Supplementary Note 14 | As shown in Supplementary Figures 17 and 18, the binding energy positions of the C 1s, N 1s, and Cu 2p orbitals in 0.7% Cu_g-CN remain largely unchanged before and after the reaction. Additionally, the Cu elemental content was measured at 1.11% before the reaction and 1.08% after the reaction, indicating minimal Cu leaching into the solution during the reaction. These results, supported by detailed elemental composition and bonding structure data (refer to Supplementary Tables 3 to 6), demonstrate the excellent stability of the catalyst.

Supplementary Table 3 | Binding energy displacement of C 1s bond structures for the different samples.

Bond structure	C/C-H	C-N	N-C=N
CN	284.8	286.23	288.19
0.7% Cu_g-CN before reaction	284.8	286.12	288.18
0.7% Cu_g-CN after reaction	284.8	286.22	288.12

Supplementary Table 4 | Binding energy displacement of N 1s bond structures for the different samples.

Bond structure	Pyridinic-N	Pyrrolic-N	Graphitic-N
CN	398.63	400.29	401.29
0.7% Cu_g-CN before reaction	399.24	400.56	401.75
0.7% Cu_g-CN after reaction	399.29	400.59	401.75

Supplementary Table 5 | Binding energy displacement of Cu 2p bond structures for the different samples.

Bond structure	Cu $2p_{3/2}$	Cu $2p_{1/2}$
0.7% Cu_g-CN before reaction	932.77	952.56
0.7% Cu_g-CN after reaction	932.7	952.47

Supplementary Table 6 | XPS elemental content (atom %) of the different samples.

Element	C%	N%	Cu%
0.7% Cu_g-CN before reaction	42.42	53.4	1.11
0.7% Cu_g-CN after reaction	40.8	54.69	1.08

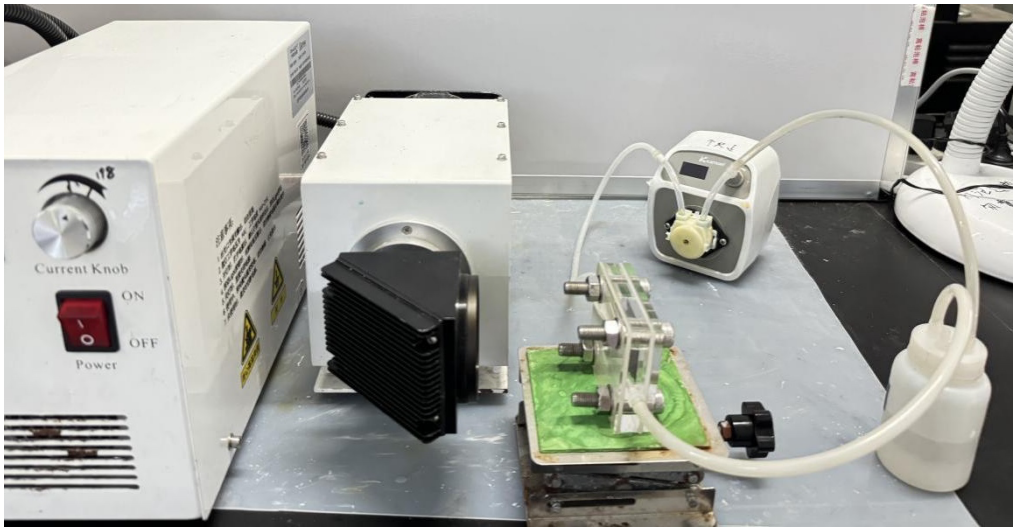

Supplementary Figure 19 | Optical pictures of the photocatalytic inactivation devices.

Supplementary Note 15 | The photocatalytic inactivation of *Chlorella vulgaris* was conducted using a flow-through apparatus, as illustrated in Supplementary Figure 19. In this setup, the photocatalysts were loaded onto 2 × 2 cm carbon paper and irradiated with a xenon lamp ($\lambda > 420$ nm) with the luminescence intensity of 1 sun as the light source.

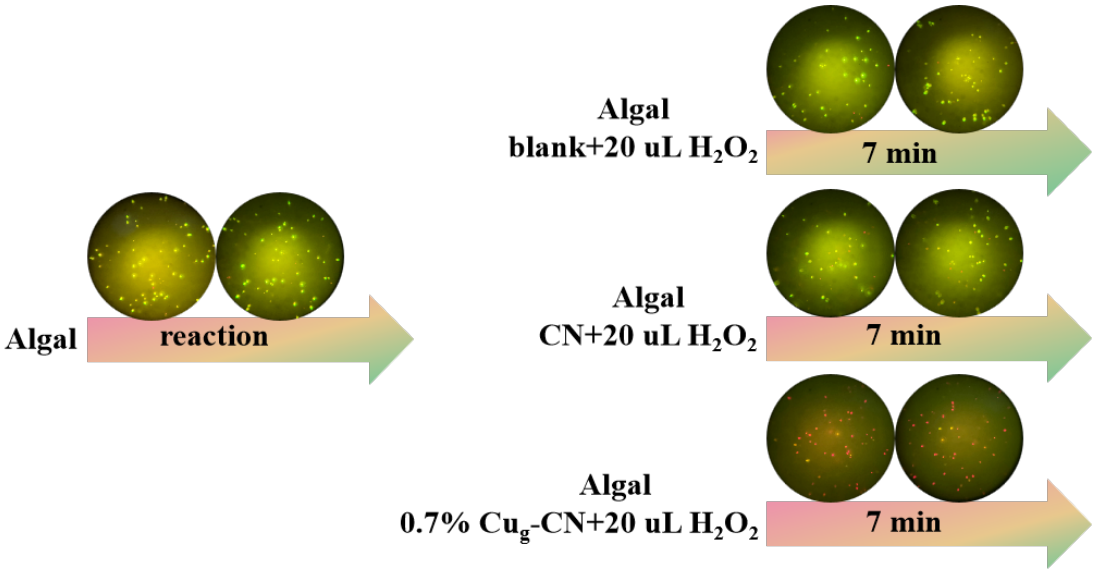

Supplementary Figure 20 | Observation of *Chlorella vulgaris* under fluorescence microscope treated with different reaction systems.

Supplementary Note 16 | In the experimental setup shown in Supplementary Figure 20, 20 μL of 30 wt.% H_2O_2 was added to evaluate the inactivation of *Chlorella vulgaris* under blank, CN, and 0.7% Cu_g-CN conditions. At the end of the reaction, a staining agent was introduced into the algal solution. Red fluorescence was observed in the dead *Chlorella vulgaris* under a fluorescence microscope, confirming the successful inactivation of the algae.

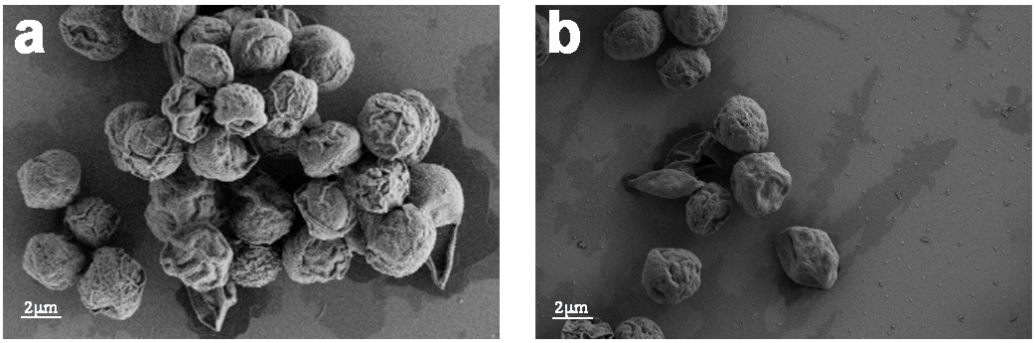

Supplementary Figure 21 | SEM image of the *Chlorella vulgaris*. a, before and **b**, the after photo-Fenton reaction.

Supplementary Note 17 | As shown in Supplementary Figure 21, the morphology of inactivated *Chlorella vulgaris* exhibited significant changes compared to untreated cells. While the surface of untreated *Chlorella vulgaris* appeared uneven and textured, the surface of inactivated cells was noticeably smoother.[42] This observation indicates that the cell membranes of inactivated *Chlorella vulgaris* were disrupted, consistent with the fluorescence microscopy results shown in Supplementary Figure 20.

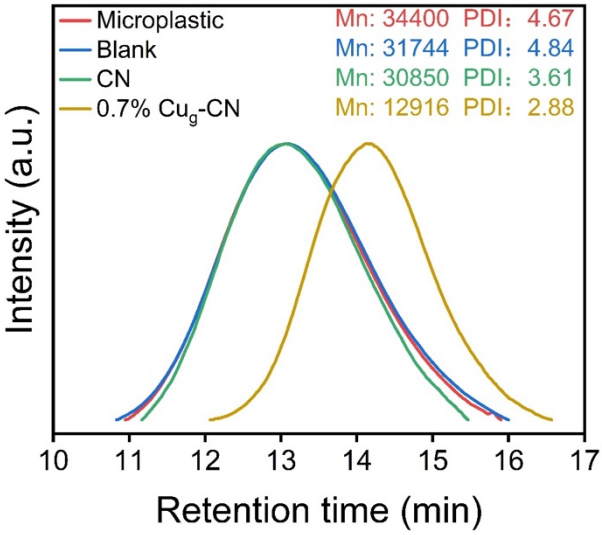

Supplementary Figure 22 | High-temperature gel permeation chromatography (GPC) measurement to quantify the degradation rate of microplastic.

Supplementary Note 18 | Supplementary Figure 22 reveals that the number average molecular mass of microplastics remained largely unchanged in the H_2O_2 and CN/H_2O_2 systems. However, in the 0.7% Cu_g-CN/H_2O_2 system, the Mn of microplastics significantly decreased to 12,916. This suggests that the abundant hydroxyl radicals generated through the photo-Fenton reaction in the 0.7% Cu_g-CN/H_2O_2 system effectively degraded the bituminous plastics.

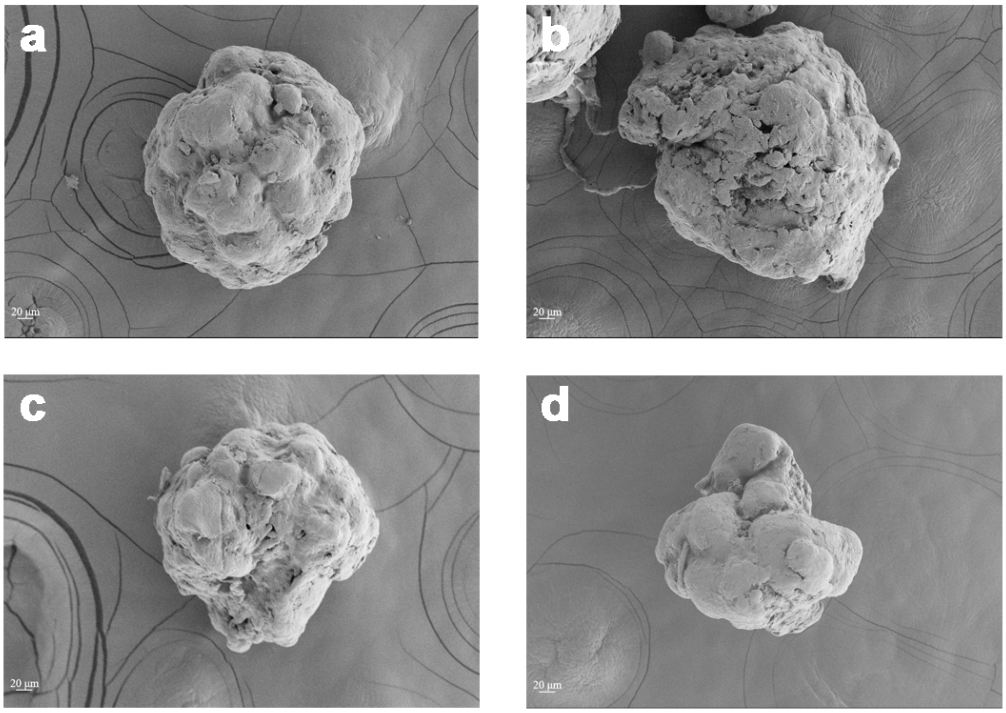

Supplementary Figure 23 | FE-SEM of microplastics under the same reaction conditions with the configuration of different catalyst. a, Microplastics as it is. **b**, H_2O_2. **c**, CN and H_2O_2. **d**, 0.7% Cu_g-CN and H_2O_2.

Supplementary Note 19 | As shown in Supplementary Figure 23, while the overall morphology of the microplastics did not change significantly, their particle size was notably reduced. This indicates that the microplastics were effectively degraded in the reaction system using the 0.7% Cu_g-CN catalyst. These findings are consistent with the results presented in Supplementary Figure 22.

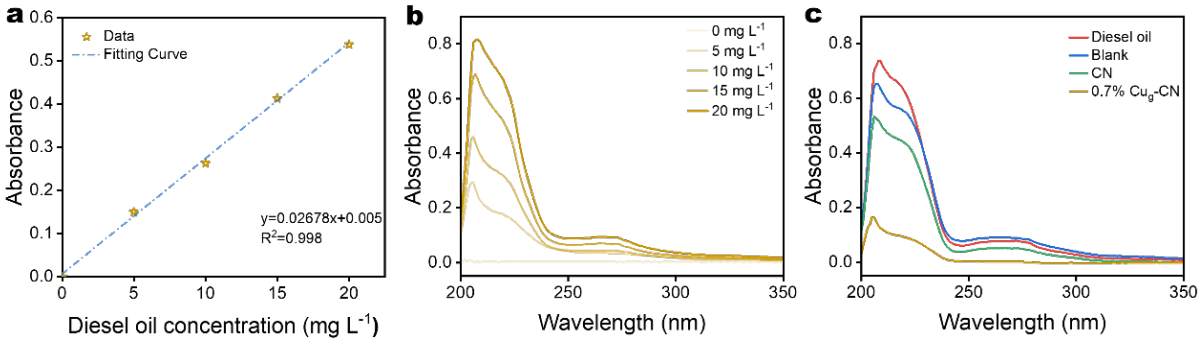

Supplementary Figure 24 | Diesel degradation performance measurement. a, UV-Vis absorption spectrum of diesel with different concentrations, which is applied as the calibration curve for the quantification of diesel concentration. **b**, Fitting curve of standard diesel-water mixture. **c**, UV-Vis spectra of diesel degradation under different reaction conditions and different catalysts.

Supplementary Note 20 | As shown in Supplementary Figure 24, the absorbance at 225 nm significantly decreased after diesel oil degradation using the 0.7% Cu_g-CN catalyst, compared to the blank group and the CN catalyst. This result indicates that the 0.7% Cu_g-CN catalyst effectively degrades diesel oil in seawater.[43]

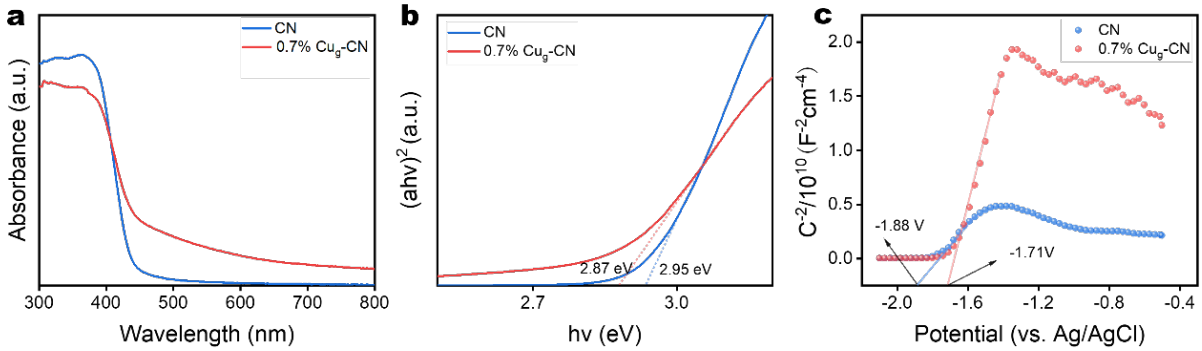

Supplementary Figure 25 | Performance analysis of light absorption efficiencies for CN and 0.7% Cu$_g$-CN. a, UV-Vis diffuse reflectance spectra (DRS) of CN and 0.7% Cu$_g$-CN. **b**, Plot of the transformed Kubelka-Munk function *versus* photon energy for CN and 0.7% Cu$_g$-CN. **c**, Mott-Schottky of CN and 0.7% Cu$_g$-CN.

Supplementary Note 21 | UV-Vis DRS spectroscopy and Mott-Schottky analysis of CN and 0.7% Cu$_g$-CN revealed no significant changes in the bandgap, valence band, or conduction band potentials of 0.7% Cu$_g$-CN compared to CN. This suggests that the enhanced catalytic performance of 0.7% Cu$_g$-CN is not attributable to improved light absorption efficiency.

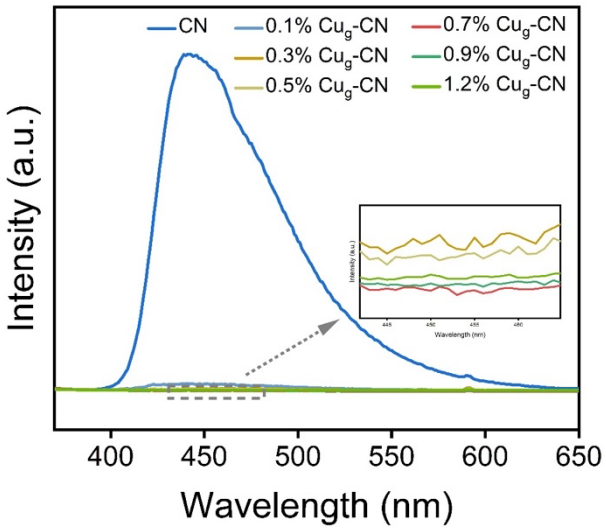

Supplementary Figure 26 | Photoluminescence spectroscopy of CN and Cu$_g$-CN.

Supplementary Note 22 | The steady-state photoluminescence (PL) intensities of photocatalysts with varying Cu synthesis ratios were compared. As shown in the figure, the CN photocatalyst exhibits the highest PL emission intensity, while the 0.7% Cu$_g$-CN sample shows the weakest emission intensity. This indicates that the rational adjustment of Cu single-atom content effectively suppresses the recombination of photogenerated carriers. Among the samples, 0.7% Cu$_g$-CN demonstrates the most significant suppression of photogenerated carrier recombination, resulting in the highest photocatalytic activity.

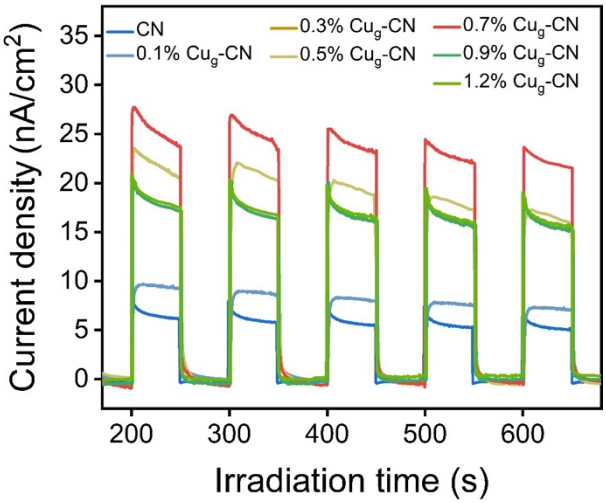

Supplementary Figure 27 | Transient photocurrent response spectra of CN and Cu$_g$-CN.

Supplementary Note 23 | Among the synthesized samples, the 0.7% Cu$_g$-CN catalyst exhibited the highest charge separation efficiency. The modulation of Cu monoatomic content effectively facilitated the separation of photogenerated electron-hole pairs, enhancing the catalyst's performance.

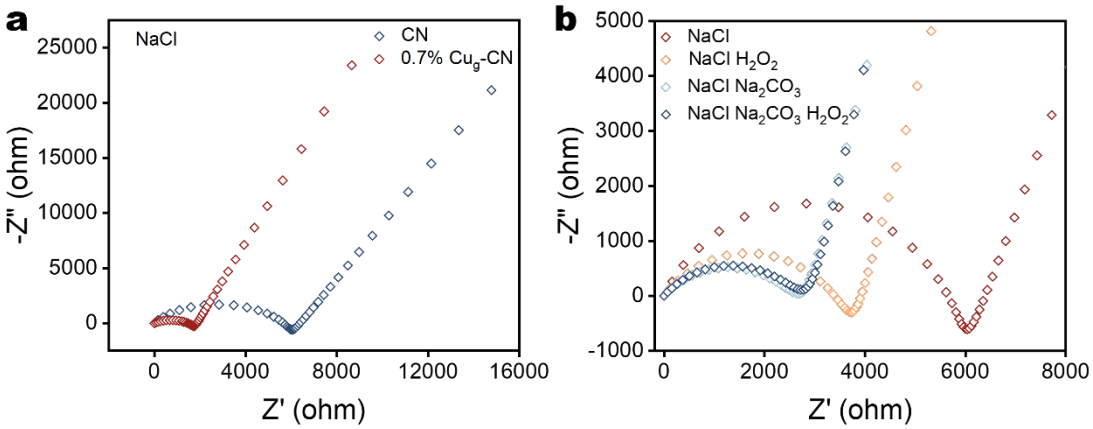

Supplementary Figure 28 | Effect of CO_3^{2-} in solution on the charge transfer efficiency of catalysts. a, EIS Nyquist plots of CN and 0.7% Cu_g-CN in NaCl solution. **b**, EIS Nyquist plots of CN with different electrolytes.

Supplementary Note 24 | To investigate the effect of ionic concentration in the solution on the EIS performance of the catalyst, the EIS test of CN was conducted in different solutions. In NaCl solution, the Rct value of 0.7% Cu_g-CN was lower than that of CN, indicating that the introduction of Cu monoatom reduced the charge transfer resistance of the material and enhanced electron mobility. The EIS results of CN revealed a decrease in R_{ct} when H_2O_2 was present in the solution. This reduction could be attributed to the inhibition of photogenerated carrier recombination, as H_2O_2 acts as an electron acceptor. Furthermore, when H_2O_2 and CO_3^{2-} coexisted, R_{ct} decreased further. This was likely due to the increased ionic concentration in the solution caused by CO_3^{2-}, which mitigated charge accumulation at the catalyst-solution interface. Interestingly, this behavior contrasted with the EIS results for 0.7% Cu_g-CN, which exhibited the opposite trend. This suggests that the observed anomaly is not related to ionic concentration but may instead be caused by CO_3^{2-} occupying the copper sites. Impedance fitting parameters and equivalent circuits are provided in Supplementary Table 7.

Supplementary Table 7. R_s and R_{ct} values for the samples under the configuration of different electrolytes.

Sample	R	solution environment	R value
CN	R_s	NaCl	102.1
		$NaCl+H_2O_2$	101.6
		$NaCl+Na_2CO_3$	100.8
		$NaCl+Na_2CO_3+H_2O_2$	103.6
	R_{ct}	NaCl	5592
		$NaCl+H_2O_2$	3453
		$NaCl+Na_2CO_3$	2937
		$NaCl+Na_2CO_3+H_2O_2$	1914
0.7% Cu_g-CN	R_s	NaCl	101.6
		$NaCl+H_2O_2$	101.1
		$NaCl+Na_2CO_3$	103.2
		$NaCl+Na_2CO_3+H_2O_2$	102.6
	R_{ct}	NaCl	1662
		$NaCl+H_2O_2$	522.3
		$NaCl+Na_2CO_3$	1029
		$NaCl+Na_2CO_3+H_2O_2$	643.9

The figure below shows the equivalent circuit used for EIS fitting (R1 denotes R_s, R2 donets R_{ct}).

equivalent circuit:

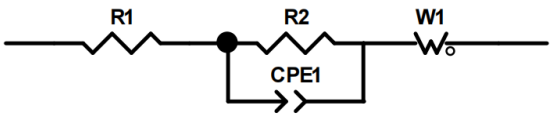

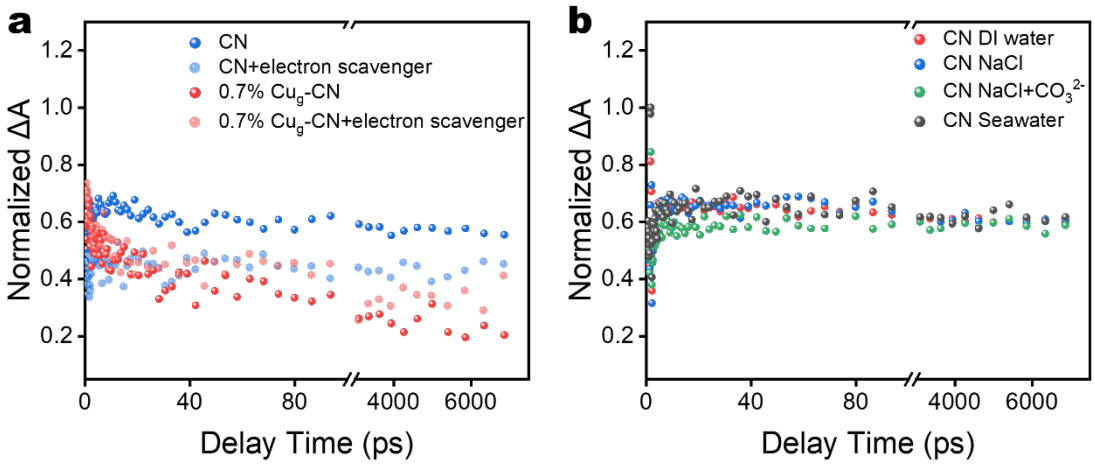

Supplementary Figure 29 | fs-TA decay intensity curves of CN and 0.7% Cu$_g$-CN **with different electrolytes. a**, fs-TA decay intensity curves of CN and 0.7% Cu$_g$CN in the electrolytes with an electron-hole scavenger. **b**, fs-TA decays intensity curves of CN with different electrolytes.

Supplementary Note 25 | To eliminate the influence of CO_3^{2-} on CN and to clarify the direction of electron transfer in the 0.7% Cu$_g$-CN material, the fs-TA decay intensity of CN and 0.7% Cu$_g$-CN with different electrolytes was analyzed. Upon adding the electron sacrificial agent ($AgNO_3$), the signal intensity of the Cu$_g$-CN samples aligned with that of the CN samples. Moreover, the signal intensity of the Cu$_g$-CN samples remained largely unchanged after the addition of the sacrificial agent. This indicates that the electrons in CN preferentially transfer to the Cu site rather than interacting with the sacrificial agent, suggesting that Cu serves as the active site for H_2O_2 conversion. Additionally, the signal intensity and decay trends of CN samples were consistent across different solutions, demonstrating that CO_3^{2-} does not affect the carrier separation efficiency of CN.

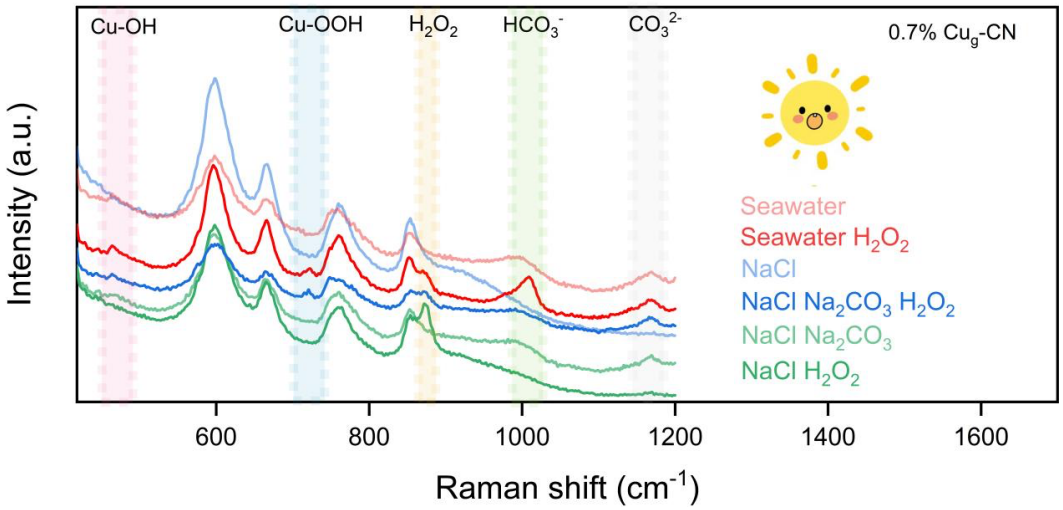

Supplementary Figure 30 | The Raman spectrums of 0.7% Cu_g-CN in different solution systems under the illumination conditions.

Supplementary Note 26 | We conducted a Raman spectroscopy analysis to further elucidate the molecular-level transformation process of H_2O_2 on Cu reaction sites in the presence of CO_3^{2-}. When CO_3^{2-} was absent from the solution, the Cu-OH peak at 464 cm^{-1} was observed, while the Cu-OOH peak at 871 cm^{-1} was not detected. In contrast, when only CO_3^{2-} was present in the solution, the Raman spectrum revealed a prominent CO_3^{2-} peak at 1165 cm^{-1}, while the HCO_3^- peak at 1009 cm^{-1} was not observed. These experimental results align with theoretical calculations, supporting the proposed mechanistic insights.

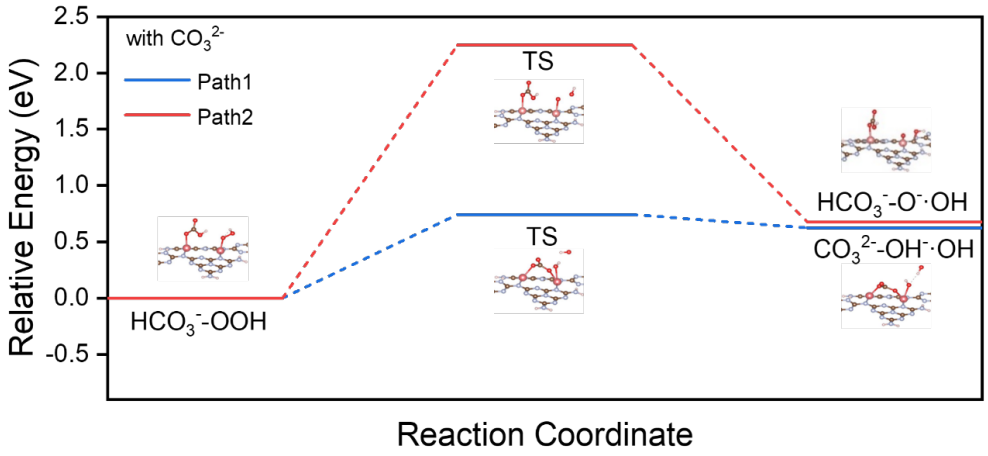

Supplementary Figure 31 | Free energy diagram for *OOH decomposition with adsorbed CO_3^{2-}. Along with the reaction pathways and corresponding atomic configurations of *OOH under the influence of adsorbed CO_3^{2-}.

Supplementary Note 27 | To further investigate the mechanism of *OOH conversion to ·OH, theoretical calculations were conducted to analyze the effect of CO_3^{2-} in solution. The results revealed that in the presence of CO_3^{2-}, *OOH preferentially acquires protons from HCO_3^- to form ·OH. This is attributed to the hydrolysis of CO_3^{2-}, which generates HCO_3^- in the solution.

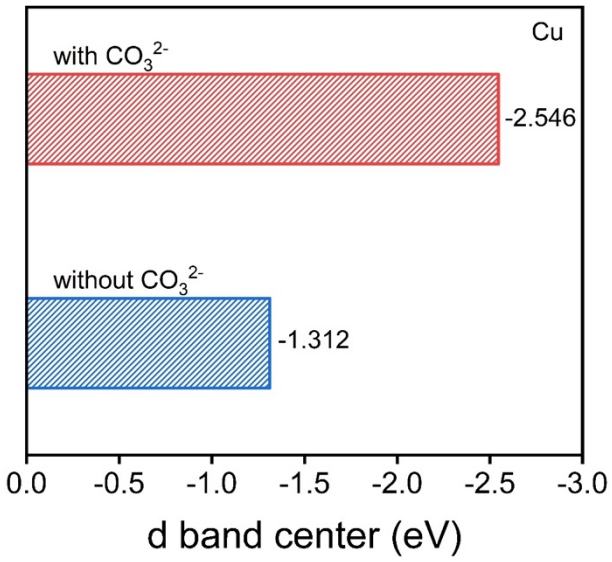

Supplementary Figure 32 | The d-band centers of Cu atoms with and without CO_3^{2-} adsorption.

Supplementary Note 28 | It can be observed that the d-band center of Cu shifts negatively when carbonate ions are adsorbed onto the Cu site. Specifically, the d-band center of Cu changes from -1.312 to -2.546, indicating a significant negative shift. In the presence of CO_3^{2-} in the solution, the electron density near the O-O bond in Cu-OOH decreases, making the bond more susceptible to breakage. Simultaneously, the ability of Cu to lose electrons is weakened, which aligns with the results of the fs-TA tests.

Supplementary References:

1. Zhang, J. & Nosaka, Y. Quantitative detection of OH radicals for investigating the reaction mechanism of various visible-light TiO_2 photocatalysts in aqueous suspension. *J. Phys. Chem. C* **117**, 1383-1391 (2013).
2. Leandri, V., Gardner, J. M. & Jonsson, M. Coumarin as a quantitative probe for hydroxyl radical formation in heterogeneous photocatalysis. *J. Phys. Chem. C* **123**, 6667-6674 (2019).
3. Louit, G. *et al.* The reaction of coumarin with the OH radical revisited: Hydroxylation product analysis determined by fluorescence and chromatography. *Radiat. Phys. Chem.* **72**, 119-124 (2005).
4. Dainton, F. S. & Watt, W. S. The effect of pH on the radical yields in the γ-radiolysis of aqueous systems. *Nature* **195**, 1294-1296 (1962).
5. Mao, W. *et al.* Bioaccumulation and toxicity of perfluorooctanoic acid and perfluorooctane sulfonate in marine algae *chlorella* sp. *Sci. Total Environ.* **870**, 161882 (2023).
6. Pozzobon, V. *et al.* Machine learning processing of microalgae flow cytometry readings: Illustrated with *chlorella* vulgaris viability assays. *J. Appl. Phycol.* **32**, 2967-2976 (2020).
7. Serra-Maia, R., Bernard, O., Gonçalves, A., Bensalem, S. & Lopes, F. Influence of temperature on *chlorella* vulgaris growth and mortality rates in a photobioreactor. *Algal Res.* **18**, 352-359 (2016).
8. Blöchl, P. E. Projector augmented-wave method. *Phys. Rev. B* **50**, 17953-17979 (1994).
9. Li, W., Walther, C. F. J., Kuc, A. & Heine, T. Density functional theory and beyond for band-gap screening: Performance for transition-metal oxides and dichalcogenides. *J. Chem. Theory Comput.* **9**, 2950-2958 (2013).
10. Chen, F. *et al.* Embedding electronic perpetual motion into single-atom catalysts for persistent fenton-like reactions. *Proc. Natl. Acad. Sci.* **121**, e2314396121 (2024).
11. Chang, Y. Fourier transform infrared (FTIR) analysis of copper oxide thin films prepared by metal organic chemical vapor deposition (MOCVD). *MRS Proc.* **293**, 443 (1992).
12. Yang, T. *et al.* Coordination tailoring of Cu single sites on C_3N_4 realizes selective CO_2 hydrogenation at low temperature. *Nat. Commun.* **12**, 6022 (2021).
13. Xing, G. *et al.* Reconstruction of highly dense Cu-N_4 active sites in electrocatalytic oxygen reduction characterized by operando synchrotron radiation. *Angew. Chem. Int. Edit.* **61**, e202211098 (2022).
14. Ravel, B. & Newville, M. *Athena* , *Artemis* , *Hephaestus*: data analysis for X-ray absorption

spectroscopy using *IFEFFIT*. *J. Synchrotron Radiat.* **12**, 537-541 (2005).

15. Duan, Y. *et al.* Simultaneous CO_2 and H_2O activation *via* integrated Cu single atom and N vacancy dual-site for enhanced CO photo-production. *Adv. Funct. Mater.* **33**, 2301729 (2023).
16. Feng, N. *et al.* Understanding the high photocatalytic activity of (B, Ag)-codoped TiO_2 under solar-light irradiation with XPS, solid-state NMR, and DFT calculations. *J. Am. Chem. Soc.* **135**, 1607-1616 (2013).
17. Ye, Z. *et al.* Surfactant-free synthesis of spiky hollow Ag-Au nanostars with chemically exposed surfaces for enhanced catalysis and single-particle SERS. *JACS Au* **2**, 178-187 (2022).
18. Qin, L. *et al.* Interlayer single-atomic Fe-N_4 sites on carbon-rich graphitic carbon nitride for notably enhanced photo-fenton-like catalytic oxidation processes towards recalcitrant organic micropollutants. *Appl. Catal. B-Environ.* **345**, 123695 (2024).
19. Torres-Ochoa, J. A. *et al.* Peak-fitting of Cu 2p photoemission spectra in Cu^0, Cu^{1+}, and Cu^{2+} oxides: A method for discriminating Cu^0 from Cu^{1+}. *Appl. Surf. Sci.* **622**, 156960 (2023).
20. Wang, A. *et al.* Direct reaction between silicon and methanol over Cu-based catalysts: Investigation of active species and regeneration of CuCl catalyst. *RSC Adv.* **8**, 19317-19325 (2018).
21. Grätzel, M. Dye-sensitized solar cells. *J. Photoch. Photobio. C* **4**, 145-153 (2003).
22. Ren, Y., Yu, J., Zhang, J., Lv, L. & Zhang, W. An in-situ strategy to analyze multi-effect catalysis in iron-copper bimetals catalyzed fenton-like processes. *Appl. Catal. B-Environ.* **299**, 120697 (2021).
23. Ren, Y. *et al.* Enhancing the fenton-like catalytic activity of nFe_2O_3 by MIL-53(Cu) support: A mechanistic investigation. *Environ. Sci. Technol.* **54**, 5258-5267 (2020).
24. Ding, R. *et al.* Oxygen vacancy on hollow sphere $CuFe_2O_4$ as an efficient fenton-like catalysis for organic pollutant degradation over a wide pH range. *Appl. Catal. B-Environ.* **291**, 120069 (2021).
25. Ling, C. *et al.* Atomic-layered Cu_5 nanoclusters on FeS_2 with dual catalytic sites for efficient and selective H_2O_2 activation. *Angew. Chem. Int. Edit.* **61**, e202200670 (2022).
26. Wang, Y., Zhao, H., Li, M., Fan, J. & Zhao, G. Magnetic ordered mesoporous copper ferrite as a heterogeneous fenton catalyst for the degradation of imidacloprid. *Appl. Catal. B-Environ.* **147**, 534-545 (2014).
27. Yu, D. *et al.* Electronic structure modulation of iron sites with fluorine coordination enables ultra-effective H_2O_2 activation. *Nat. Commun.* **15**, 2241 (2024).

28. Zhan, H., Zhou, R., Wang, P. & Zhou, Q. Selective hydroxyl generation for efficient pollutant degradation by electronic structure modulation at Fe sites. *Proc. Natl. Acad. Sci.* **120**, e2305378120 (2023).
29. Lv, X. *et al.* Construction of a visible-light-response photocatalysis-self-fenton degradation system of coupling industrial waste red mud to resorcinol-formaldehyde resin. *Molecules* **29**, 1514 (2024).
30. Li, L., Hu, C., Zhang, L. & Shi, B. More octahedral Cu^{+} and surface acid sites in uniformly porous Cu-Al_2O_3 for enhanced fenton catalytic performances. *J. Hazard. Mater.* **406**, 124739 (2021).
31. Yin, Y., Lv, R., Li, X., Lv, L. & Zhang, W. Exploring the mechanism of ZrO_2 structure features on H_2O_2 activation in Zr-Fe bimetallic catalyst. *Appl. Catal. B-Environ.* **299**, 120685 (2021).
32. Zhang, T. *et al.* Homogeneous carbon dot-anchored Fe(III) catalysts with self-regulated proton transfer for recyclable fenton chemistry. *JACS Au* **3**, 516-525 (2023).
33. Sun, M. *et al.* Reinventing fenton chemistry: Iron oxychloride nanosheet for pH-insensitive H_2O_2 activation. *Environ. Sci. Technol. Lett.* **5**, 186-191 (2018).
34. Huang, Q., Liu, H., Huang, M., Wang, J. & Yu, H. Ligand-assisted heterogeneous catalytic H_2O_2 activation for pollutant degradation: The trade-off between coordination site passivation and adjacent site activation. *Appl. Catal. B-Environ.* **330**, 122592 (2023).
35. Tian, L. *et al.* Enhanced degradation of enoxacin using ferrihydrite-catalyzed heterogeneous photo-fenton process. *Environ. Res.* **251**, 118650 (2024).
36. Yu, H. *et al.* Facile preparation of coprecipitates between iron oxides and dissolved organic matter for efficient fenton-like degradation of norfloxacin. *J. Hazard. Mater.* **444**, 130394 (2023).
37. Yamaguchi, R., Kurosu, S., Suzuki, M. & Kawase, Y. Hydroxyl radical generation by zero-valent iron/Cu (ZVI/Cu) bimetallic catalyst in wastewater treatment: Heterogeneous fenton/fenton-like reactions by fenton reagents formed in-situ under oxic conditions. *Chem. Eng. J.* **334**, 1537-1549 (2018).
38. Zhong, Q., Li, Y., Liu, J., Li, J. & Zhang, G. In situ construction of Ti^{3+} self-doped TiO_2/Ti_3C_2 schottky heterojunctions for highly selective photo-fenton-like degradation of organic pollutants: Surface/interface effect and mechanism insight. *Appl. Surf. Sci.* **667**, 160376 (2024).
39. Qian, M. *et al.* Modulation of charge trapping by island-like single-atom cobalt catalyst for enhanced photo-fenton-like reaction. *Adv. Funct. Mater.* **33**, 2208688 (2023).
40. Tan, Z. *et al.* Highly efficient electrocatalysis of oxygen to hydroxyl radical by FeN_2O_2 single-

atom catalyst for refractory organic pollutant removal. *Appl. Catal. B-Environ.* **355**, 124170 (2024).

41. Zhou, Y., Yu, M., Zhang, Q., Sun, X. & Niu, J. Regulating electron distribution of Fe/Ni-N_4P_2 single sites for efficient photo-fenton process. *J. Hazard. Mater.* **440**, 129724 (2022).
42. Peng, Y. *et al.* Biological activity and molecular mechanism of inactivation of microcystis aeruginosa by ultrasound irradiation. *J. Hazard. Mater.* **468**, 133742 (2024).
43. Hu, D. D., Yu, X. C., Zhang, M., Guo, J. Y. & Zheng, X. Study on the photocatalytic degradation of diesel pollutants in seawater by a sonochemically prepared nano zinc oxide. *Adv. Mater. Res.* **476-478**, 1939-1942 (2012).